Rise-times of Core-Collapse Supernovae

MSc thesis
University of Turku
Astronomy
2024
BSc Maija Rikala
Supervisor:
Dr. Claudia P. Gutiérrez
Prof. Seppo Mattila
Examiners:
Prof. Seppo Mattila
Dr. Hanindyo Kuncarayakti

The originality of this thesis has been checked in accordance with the University of Turku quality assurance system using Turnitin Originality Check service.

UNIVERSITY OF TURKU
Department of Physics and Astronomy

Rikala, Maija Rise-times of Core-Collapse Supernovae

MSc thesis, 61 pages
Astronomy
February 2025

A supernova is the explosive end of a star. If the star is a white dwarf in a binary system, the supernova will be a thermonuclear or type Ia supernova. On the other hand, if the dying star is a massive star, the supernova will be a core-collapse supernova. In this kind of supernova, the star's core collapses under its own gravity after the fusion chain in its core reaches iron because its fusion consumes rather than generates energy. This collapse releases large amounts of energy. The collapse and the radioactive isotopes produced in the explosion power the supernova to emit radiation that we can observe. Core-collapse supernovae and their photometry are the main focus of this thesis.

When the luminosity of a supernova is observed over time, the observations can be used to plot the supernova's light curve. By studying the light curve, the time from the explosion to the peak luminosity, i.e., the rise-time, can be determined.

In this thesis, a sample of supernovae was studied and their rise-times investigated. Different supernova types evolve differently, so their rise-times also vary. Supernova rise-times can help in the investigation of progenitor characteristics, which are still not fully understood. Similarly, the understanding of the explosion mechanisms is still incomplete.

This thesis aims to give some insight into the rise-times of core-collapse supernovae of different subtypes. Both stripped-envelope (Ib, Ibn, Ic, Ic-BL) and hydrogen rich (II, IIn) as well as the intermediate type (IIb) are studied. In addition to the rise-times, peak magnitudes and a subsample of more peculiar supernovae are identified. The peak magnitudes are plotted against rise-times to find possible correlations. The peculiar subsample offers a peek at the diversity of supernova light curve shapes, which could motivate further research.

Keywords: supernova, core-collapse, rise-time, light curve

Contents

1 Introduction

1.1 A core-collapse supernova explosion

The light that we see from the Sun and all the stars in the night sky is produced deep inside these massive objects that look very small and peaceful due to their incredible distance. They are held together by their own crushing gravity that is countered by internal pressure produced by fusion reactions in the core. Fusion produces heavier elements from lighter ones, which releases energy. These reactions create a chain of elements with increasing mass, and for more massive stars, the chain is longer. This is because fusing higher-mass elements together requires higher pressure and temperature, and this is possible only in the cores of higher-mass stars. Gravity and pressure are in balance for as long as the fusion continues creating energy, and the star can continue living its relatively peaceful main-sequence life.

Once a massive star - one that initially has more than 8 times the mass of our Sun - reaches fusion of iron, the process starts to consume energy instead of generating it. The process also consumes electrons that help keep up the internal pressure with their degeneracy pressure. This marks the end of the star's life. The pressure is needed to keep the star in balance, and as the energy release ceases, gravity wins. Fusing iron will lead to the collapse of the star's core, which happens on a timescale of less than a second. During the collapse, pressure will naturally increase, leading to protons capturing electrons and the photodissociation of iron, releasing neutrinos, which carry most of the energy released in the explosion [1].

As the core shrinks, the outer layers of the star lose their support and fall inwards, bouncing outward. A shock wave will propagate through the star's envelope. The rebound would not be enough to create the explosion, as the material would eventually fall back to the core. The key are the neutrinos, as some of them are absorbed by the outer layers, and this drives outward explosion ([1], [2]) or at least this

is the current leading theory. Either way, the result is a supernova (SN) explosion.

The core can become a neutron star because electron capture produces large amounts of neutrons, which increases the core's density to the point of matter becoming degenerate. If the mass of the core is high enough or because some of the expanding material falls down and is accreted by the core, it can become a black hole. This happens, if the core's mass exceeds the Tolman-Oppenheimer-Volkoff limit, which, depending on the calculation method, is roughly $1.5M_{\odot}$ to $3.0M_{\odot}$, where $M_{\odot}$ is the solar mass. Kalogera and Baum [3] found the upper limit for a neutron star to be $2.2M_{\odot}$ - $2.9M_{\odot}$.

The first visible sign of the explosion we can observe is a shock breakout (SBO): a flash of radiation in X-ray and UV that lasts from seconds to hours. Bersten et al. [4] showed that a SBO can extend to the optical range as well. In a SBO, optical depth ahead of a moving shock wave decreases, and once it is below c/v_{shock} (c being the speed of light and v_{shock} being the speed of the shock), radiation escapes. This happens at the outer edge of the star [5]. A SBO is often so short that it isn't observed at all as it can last a few hours or even less. Still, if there is a large amount of circumstellar material (CSM) around the exploding star, the SBO might be delayed and increase the duration to several days [5], [6]. After the SBO, the deeper parts of the SN become visible as radiation deeper from the star escapes.

The main powering mechanism of a SN is the decay of radioactive nickel isotope ^{56}Ni and its decay product ^{56}Co produced in the explosion. The half-life of the first is about 6 days [7] and the half-life of the second about 77 days [8]. The effect of these can be seen in the main peak and tail after SBO.

The shape of a SN light curve (LC) is demonstrated in figure 1, where SN 1993J serves as an example. On y-axis is apparent magnitudes and on x-axis is time in modified Julian dates (MJD). Julian date is the number of days since noon Universal Time in fist of January 4713 BCE and MJD is Julian date minus 2 400 000.5 days.

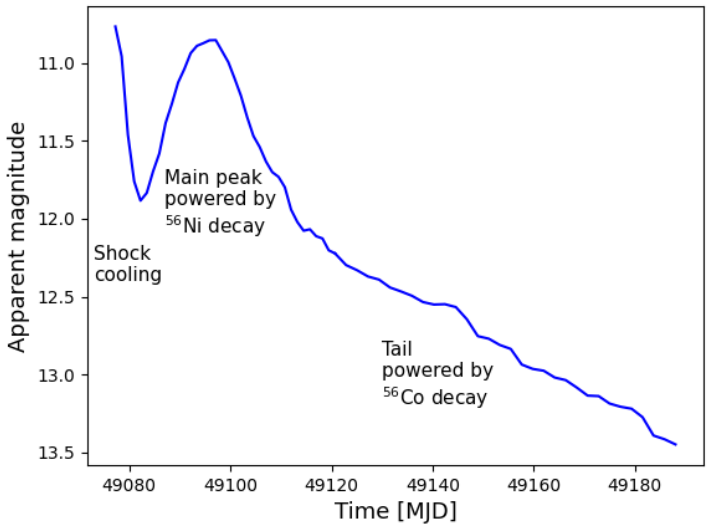

Figure 1. LC of SN 1993J to demonstrate the shape of a SN LC. The first visible feature is the falling curve, which is due to the shock cooling, after which the decay of ^{56}Ni powers the LC during the main peak. It decays to ^{56}Co, which decays and powers the tail. Data from [9], [10], [11], [12], [13], [14], [15], [16].

In figure 1 the SBO is not visible since it happened too quickly to observe in time, but the shock cooling can be seen as the first declining slope in the LC. The shock heats up the material as it propagates through, leaving it to cool down. When this happens, the radiation peak moves to optical range, and we see an increase in the LC as the so called shock cooling phase. Then, the decay of ^{56}Ni starts to dominate the LC, which can be seen as the main peak. It decays into ^{56}Co, and its decay powers the tail of the LC. This, however, is only one example, and in reality, SNe have a wide variety of LC shapes.

The time from the explosion to the main peak is defined as the rise-time. However, the rise-time of a single SN varies depending on the wavelength used, i.e., the band. As the photosphere temperature decreases with time, the emission peak from the SN moves towards longer wavelengths. Therefore, the peak luminosity moves toward redder bands with time, and the peak occurs at different times depending on the band [17], [18].

In addition to the main peak, there can be multiple peaks in a LC due to different physical mechanisms. If there is a large amount of slow-moving CSM around the star, fast-moving ejecta will collide and interact with it, transforming kinetic energy into radiation [6]. An eruption before the actual explosion can show up as a smaller bump in the LC before the actual peak. This kind of precursor is common with type IIn SNe [19]. A neutron star with a strong magnetic field, i.e. a magnetar can also power the LC through its magnetic fields (e.g. [20]).

1.2 Classification of supernovae

Supernovae (SNe) described above are core-collapse (CC) SNe, and they are the main focus of this thesis. In addition to CCSNe, there are also thermonuclear SNe, known as type Ia SNe. Their explosion mechanism is different as they are not massive stars but rather white dwarfs that explode due to accreting matter from a companion star in a binary system [21]. They are known as standard candles and are used to measure the expansion of the universe.

In addition to SNe Ia, there are many other classifications. These are the CCSNe [22] since only type Ia SNe (and subclasses) make up the thermonuclear SNe. The classification of SNe began in 1941 when Rudolph Minkowski published his article that became the basis of future SN classification [23]. He divided SNe into two groups based on whether they had hydrogen features in their spectra (type II SNe) or not (type I). Later, further subclassifications have been made.

If a type I SN has prominent He lines in its spectra, it is classified as a type Ib SN [24]. If these He lines are narrow emission lines, they likely come from a He-rich CSM around the star [25], and these events are labelled as type Ibn SNe. Here, the 'n' stands for narrow.

Another subclass of type I are SNe Ic. They have neither He features nor the prominent 6150 Å Si II line in their spectra [26], which is a distinct feature in Ia

SNe [27]. Some type Ic SNe display highly broadened spectral features due to the very high velocities of the ejecta. These SNe are called SNe Ic-BL, and 'BL' stands for the broad line.

Two subclasses of classical SNe are defined by their photometric properties instead of spectroscopic ones. These are II-P and II-L SNe, where P stands for plateau and L for linear. As their names suggest, SNe II-P are defined by a period of almost constant luminosity, whereas SNe II-L have an approximate linear decline in their LC in magnitude space [28]. For example, Arcavi et al. [29] argued, using a sample of 21 type II SNe, that the plateau length of a type II-P SN is roughly uniform at 100 days. Later, however, Anderson et al. [30], Galbany et al. [31], and Sanders et al. [32] investigated larger samples of type II-P and II-L SNe. They did not find evidence for distinct groups but rather a continuum of plateau lengths. Thus, all SNe classified as either II-P or II-L are combined here and will be labelled as SNe II.

In addition to type II-P and II-L, type II-pec are defined by their LCs, and they have a differing or peculiar LC shape compared to the other two. Most type II SNe have a decline in their LCs after the shock breakout, but SNe II-pec instead have a slow rise to their peak [33].

Some SNe have H lines in their spectra at early times, but as they evolve, their H features disappear, and He I lines become visible. Thus, they begin to resemble type Ib SNe at later times. These SNe have been labelled as SNe IIb [34].

Finally, Schlegel [35] introduced the subclass SNe IIn. These are type II SNe with narrow hydrogen emission lines in their spectra, much like the case of SNe Ibn. These emission lines are caused by the ejecta's interaction with the surrounding CSM.

The progenitors of SNe Ia are white dwarfs, and the progenitors of CCSNe are massive stars. Typical progenitors of type II SNe are red supergiant stars [18]. Gal-Yam & Leonard [36] showed that a luminous blue variable (LBV) could also be the

origin of a SN. Wolf-Rayet stars are also thought to be possible progenitors of SE SNe [37]. Arnett et al. [38] demonstrated that a blue supergiant star could explode as a SN in the case of SN 1987A and other objects like it, despite disagreement with theory. SN 1987A is well studied SN that exploded in the Large Magellanic Cloud, and it was characterised by its long rise-time, as it took more than three months to reach its peak.

1.3 Research today

This thesis relies on the observational data from Zwicky Transient Facility (ZTF) [39], [40] and Asteroid Terrestrial-Impact Last Alert System (ATLAS) [41], [42].

ZTF is an optical survey dedicated to observing a large variety of astronomical objects, including SNe. The survey started its operations in 2018 as the successor of the Intermediate Palomar Transient Factory (iPTF) and Palomar Transient Factory (PTF) before that. ZTF scans the entire northern sky every two to three days and uses the Palomar 48-inch Samuel Oschin Schmidt Telescope in its observations. ZTF has limiting magnitudes of 20.8 in the g-band, 20.6 in the r-band and 19.9 in the i-band [39].

ATLAS is another optical survey that scans the whole sky every two nights to search for moving objects and especially to provide warning in case of a possible asteroid collision with Earth. These scans, of course, capture much more than just potential asteroid threats, as they have a limiting magnitude of about 19.7. ATLAS uses two independent 0.5 m Schmidt telescopes in Haleakala and Mauna Loa in Hawaii [41], [42].

Finally, one might ask why the rise-times of CCSNe are important to research. The physics behind the progenitors and the early phases of SNe are not fully understood. Rise-times can help, as they offer information about the progenitors' characteristics and possible mass-loss history. For example more compact progeni-

tors have longer rise-times, as they spend more energy on expanding their envelopes during the explosion. Also if a progenitor has lost a large amount of mass before explosion, this can show as a luminous peak in the LC. Not many studies have been done on the rise-times of all classical CC SN types, so this will serve to fill that gap.

In addition, there are multiple surveys, such as ZTF, ATLAS, All Sky Automated Survey for SuperNovae (ASAS-SN) [43], Palomar Transient Factory (PTF) [44] and Panoramic Survey Telescope and Rapid Response System (Pan-STARRS) [45] that are dedicated to photometric observations. Spectroscopic information is more challenging since these measurements require longer exposure times. Thus, relying more on photometric data, such as rise-times, is needed. Classification of SNe has relied on spectroscopic information, but rise-times could become a valuable tool to aid classification. For example, Förster et al. [6] used early LCs of 18 SNe to divide them into either type Ia or II SNe. With spectroscopic information, they validated that the classification was accurate. With more research, this process could be refined and become more useful.

Though the main subject of this thesis is the rise-times of CCSNe, a subsample of peculiar SNe was identified based on their photometry. They are also addressed briefly.

2 Sample

This study's sample consisted of 212 CCSNe selected from 2019. This year was chosen because there would be a sufficient number of classifications for the SNe, and a long enough time had passed since the explosion, so there would be a significant number of observations available. This ensured a large enough sample for the study.

The SNe in this sample were selected based on the following criteria: all of the SNe had to have spectroscopic classifications of classical CCSNe, and they needed to have a good number of observations. Classical CCSN here means that the supernova

isn't for example a superluminous SN, which - as its name suggests - is a more luminous SN than the more commonly observed SN types. For example Gal-Yam [46] defines superluminous SNe as SNe with observed peak absolute magnitudes as $M < -21$ in any band.

The sample was divided into four subsamples. The gold sample criterion was that there had to be a well-defined rise and peak in at least two bands. This means there had to be a deep non-detection (more details in Section 3.1) within 20 days of the first detection, so the error of the explosion epoch is less than 10 days. In addition, it was required that at least two detections were recorded during the rise and in close proximity to detections after the peak so that the peak is well defined, i.e., the gap between detections must not be too long. However, this does not mean that all bands for a gold sample SN were of equal quality; the peak time in one band should also not differ largely from that of other bands. This difference is discussed more in section 4.2.

How the gold sample is defined can introduce a bias towards longer rise-times. This is because shorter rise-times are harder to observe, and it is especially difficult to have two or more detections during the rise, with the cadence being a few days. However, this definition ensures that the rise-time can reliably be defined.

In the silver sample, all of the SNe must have at least one band with at least one detection during the rise and the next close enough to define the peak.

Bronze sample included SNe that either had a well-defined peak but no deep non-detections within 20 days or a deep non-detection but no detections during the rise, in which case the peak is not defined. In these cases, lower and upper limits could be obtained for the rise-times, respectively. Only those bands that had observations close to the explosion epoch were used.

Finally, a subset of SNe had neither visible rise nor deep non-detections within 20 days. The rise-times of these SNe could not be determined, so they were discarded

Table 1. Number of SNe of each type in each subsample. The first row shows the number in the complete sample.

	Ib	Ibn	Ic	Ic-BL	II	IIb	IIn	Total
All SNe	18	4	14	6	123	10	37	212
Gold sample	8	2	9	4	40	8	22	93
Silver sample	3	2	4	2	35	1	5	52
Bronze sample	4	0	0	0	17	0	3	24
Unusable sample	3	0	1	0	31	1	7	43

from the sample. This left 169 viable SNe in the sample.

The SNe included in this sample were found on the Transient Name Server (TNS)[1]. Their spectroscopic classifications were obtained and used as final classifications except for type II-P and II-pec SNe, which were labelled as type II.

SNe in this sample includes the types Ib, Ibn, Ic, Ic-BL, II, IIb and IIn. The number of SNe of each subtype in each subsample is presented in Table 1.

Photometric data for the LCs were downloaded from ZTF forced photometry service[2] [47] and ATLAS web service[3] [48]. The data from ZTF was in g-, r-, and i-bands, though data were least regularly available in i-band. Taking from the SVO Filter Profile Service[4], these correspond to effective wavelengths 4746 Å, 6366 Å and 7829 Å, respectively. ATLAS provided data in o- and c-bands, though here again, there were fewer observations in c-band. The effective wavelengths from the same filter profile service are 6630 Å and 5182 Å, respectively.

Data from both ZTF and ATLAS was forced photometry. In this case, 'forced' means that when a certain location in the sky is imaged, the survey gets a magnitude value from the observation regardless of whether there is an object or not. Thus,

[1]https://www.wis-tns.org/

[2]https://ztfweb.ipac.caltech.edu/cgi-bin/getForcedPhotometryRequests.cgi

[3]https://fallingstar-data.com/forcedphot/

[4]http://svo2.cab.inta-csic.es/theory/fps/

a magnitude is forced, and the result is either a non-detection or a detection (see Section 3.1). Since multiple images are taken from the same location and are stacked together, the probability of detecting an existing object increases.

ZTF and ATLAS use archived reference images of each imaged part of the sky where a SN has been detected. When a new observation is made, the archived image is subtracted from the observation, and the result is the difference of the images or, in other words, flux relative to the reference image. This is called differential photometry. Since the data were downloaded in flux space from both ZTF and ATLAS, it had to be converted to magnitude space.

In general, the data from ATLAS had better quality than that from ZTF. For example, in the case of SN 2019lr, the observations from ZTF could not be used to fit a realistic or reasonable LC, but there was no problem in ATLAS o-band. The opposite was also true in a few cases, such as SN 2019gss, where the observations were so faint that they were close to the ATLAS magnitude limit.

During the preparation of the LCs, it became clear that more data were needed for a proper baseline correction (more detailed description in Section 3.3). Since this correction was necessary only for ZTF data, more data from ATLAS was not downloaded, and thus, there are fewer ATLAS epochs for most of the SNe.

The redshifts for each SN were taken from TNS, which was used to calculate the distances and distance moduli. Galactic extinction in g-, r- and i-bands [49] and visual extinction A(V) [50] values were obtained from NASA/IPAC Extragalactic Database (NED)[5].

3 Methodology

This section presents the methods used to prepare the data and what was extracted for further analysis.

[5] `https://ned.ipac.caltech.edu/`

3.1 Estimating explosion epochs

The first step was to determine the time of the explosion, i.e., the explosion epoch. To estimate it, the first detection and the last non-detection before it was taken, and their midpoint was taken as the explosion epoch.

A non-detection is an observation in which the SN could not be confidently detected. Section 3.3 presents how observations were divided into detections and non-detections. Before the explosion, there were naturally several non-detections as the SN could not yet be detected. Still, later, for example, weather conditions or a full moon could prevent a detection.

For the non-detection to be reliable, it had to be deeper than the first detection and its error. Quick plots of each SN were done to get these epochs, where observations within 24 hours were stacked together so that each observation did not need to be individually checked. Since multiple observations could be done during the same night, this simplified the plots significantly without losing too much accuracy.

Ideally, the non-detection would be in the same band as the first detection, but this was not required. For example, second to last non-detection could also be chosen if the last one was very close to the first detection and didn't provide a reliable constraint. For example, in the case of SN 2019rfi, there was only one non-detection within 20 days of the explosion. This was in the o-band, as was the first detection, but the non-detection was only marginally deeper than the detection. Thus, it was not considered a reliable constraint.

This method relies heavily on very few observations and one problem is that different surveys or even different bands in the same survey have different limiting magnitudes. Therefore, a SN might have occurred even though it is not detected, which would affect the explosion epoch estimation. The limiting magnitudes of ZTF i-band and ATLAS are close, but there is about one magnitude difference between the ZTF g- and r-band limiting magnitudes and the ATLAS limiting magnitude.

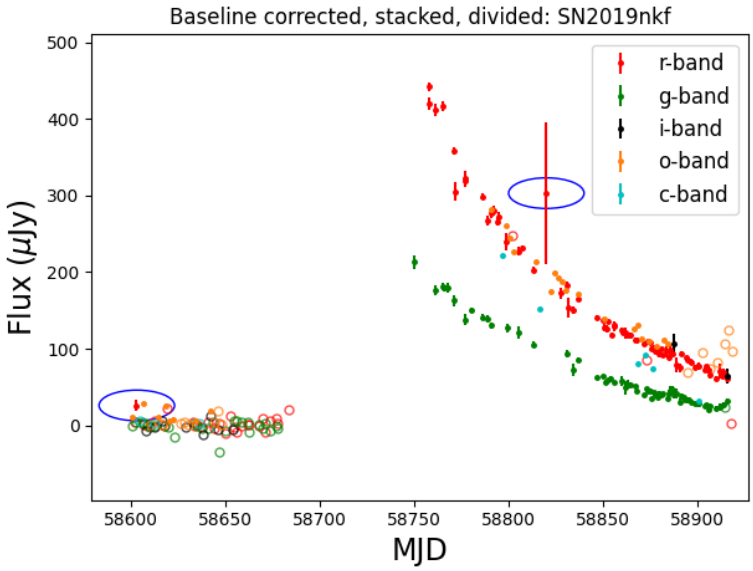

Figure 2. LC of a type Ic SN 2019nkf in flux space, which has been baseline corrected, stacked, and observations have been divided into non-detections and detections. Detections are marked with filled circles, and non-detections are marked with open circles. Two dubious detections are circled. The first one occurs at least 85 days before the explosion, so it cannot be related to the explosion. The second one has very large error bars, and the flux level is significantly higher than before and after the detection, so it is likely false.

Thus, this is a possible source of error.

Even with criteria for detections, some non-detections were marked falsely as detections and had to be ruled out by eye. If such a detection was at least 10 days before the rise, it was clearly not an indication of a SN explosion. If there were deep non-detections, especially in the same band, after detection, it would also most likely not be a real detection. Multiple bands were also considered, so if there was an ambiguous detection in only one band, it was less likely to be real. These things were considered when determining if a detection was real or not.

A computer code in flux space was used to get a better understanding of whether detection was a false or a real one. Baseline correction and stacking (explained in Section 3.3) were applied, and then data points were divided into detections and non-detections. The division was based on whether or not the flux value was at least 3σ. As an example type Ic SN 2019nkf is shown in Figure 2. In the figure, detections are

marked with filled circles and error bars, and non-detections are marked with open circles. Different bands are marked with different colours, as shown in the legend.

In this figure, there is a detection in the r-band around 58600 MJD. The r-band detection occurred long before the explosion, which must have happened sometime during the observation gap or just before. This is clear because there are many non-detections between 58600 and 58685 MJD with almost constant flux around 0. Because there is a long period when the SN has not been detected, it must not have exploded, at least long before the observation gap.

Even though the baseline is relatively well constrained to a constant flux, there is still some dispersion. The detection falls within that dispersion, making it possible that it is just a false detection. It is, however, possible that the detection is real, and this is an outburst, where the star's luminosity increases for a short period of time due to an eruption of gas, but it does not lead to the final death of the star. Either way, it does not indicate that the explosion has occurred at this time.

This code could also be used to distinguish false detections closer to the explosion epoch if they were visible. Before the explosion, the upper limits of non-detections are typically close to constant and near zero flux after baseline correction. After the explosion, the curve rises very sharply in flux space. If there were false detections before this sharp rise, they were discarded as false detections.

These false detections just before the explosion in CC and especially SE SNe could be due to precursors before the actual explosion. A precursor is an intense mass-loss event months to days before the final SN explosion of a star, which can emit large amounts of radiation. A precursor can be an outburst or a more steady stellar wind [51]. So even though these really were higher flux detections, they were not caused by the SN and, thus, not actually relevant detections. For example, there are sometimes precursors before the explosion in the case of SNe IIn [52].

Similarly, another detection in r-band is marked at 58820 MJD. During this part

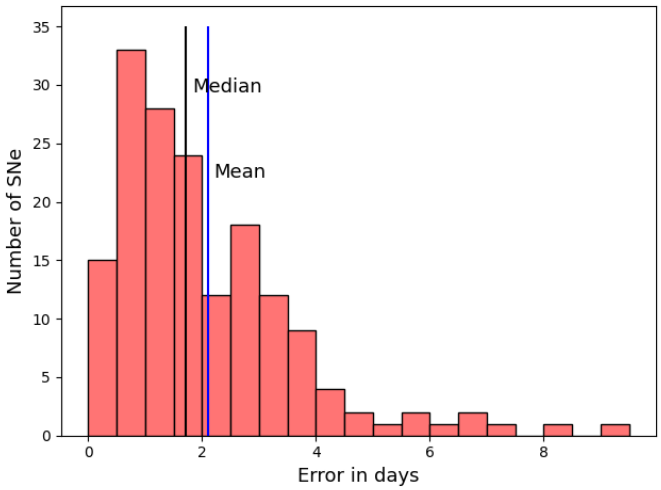

Figure 3. Distribution of uncertainties in explosion epoch estimation. The median and mean values are marked with vertical lines.

of the LC, the slope is negative, and the marked detection clearly differs from the trend. Since it has very large error bars and it is off the rest of the LC, it is discarded as a false detection.

Uncertainties obtained from explosion epoch estimation are presented in Figure 3. The uncertainty was the time between the last non-detection and the first detection divided by two. Only those SNe that had a deep non-detection within 20 days of the first detection were considered in this estimation. The vertical black line marks the median of the uncertainties, and the vertical blue line marks the mean value of the uncertainties. The median is 1.72 days, and the mean is 2.10 days.

3.2 Parameters

Redshift was used to calculate the distance of the SN using Hubble's law [53] or in practice with equation 1, which was further used to obtain the distance modulus with equation 2.

$$d = \frac{z \cdot c}{H_0} \tag{1}$$

$$\mathrm{DM} = 5 \cdot \log_{10}\left(\frac{d \cdot 10^6}{10\ \mathrm{pc}}\right) \tag{2}$$

Here $H_0 = 70$ km s^{-1}Mpc^{-1} is the Hubble constant, c is the speed of light in units km s^{-1}, z is the redshift, d is the distance in megaparsecs and DM is the distance modulus. As the Hubble constant isn't well established, this value was chosen because it is commonly used.

This equation is valid for $0.01 \lesssim z \ll 1$. In other words, when the object in question is far enough away, peculiar velocities can be ignored. The other point comes from the fact that the redshift used here comes from the Doppler effect. Specifically, it is not the same as the cosmological redshift. The first comes from the object moving through space, and the latter from the expansion of space itself.

The largest redshift of the sample is 0.285, though this belongs to an unusable SN. The largest redshift for a usable SNe is 0.125, and most are less than 0.06, as seen in Figure 4. The smallest redshift is 0.0043, which is below the lower limit, though the vast majority of redshifts are above 0.01. Because of this and the complexity of accurate distance measurements, equation 2 was used for consistency. This also does not affect the rise-time, as the distance is the same for all epochs of a single SN. It affects only the peak magnitude estimation.

As mentioned, extinction was obtained from NED[6]. Only the Milky Way extinction was considered. Since no ATLAS o- and c-band values were available, they were calculated following [54]. The equations needed were equations 3 - 6.

$$y = x - 1.82 \tag{3}$$

$$\begin{aligned} a(x) = {} & 1 + 0.17699y - 0.50447y^2 - 0.02427y^3 + 0.72085y^4 + 0.01979y^5 \\ & - 0.77530y^6 + 0.32999y^7 \end{aligned} \tag{4}$$

$$\begin{aligned} b(x) = {} & 1.41338y + 2.28305y^2 + 1.07223y^3 - 5.38434y^4 - 0.62261y^5 \\ & + 5.30260y^6 - 2.09002y^7 \end{aligned} \tag{5}$$

[6] `https://ned.ipac.caltech.edu/`

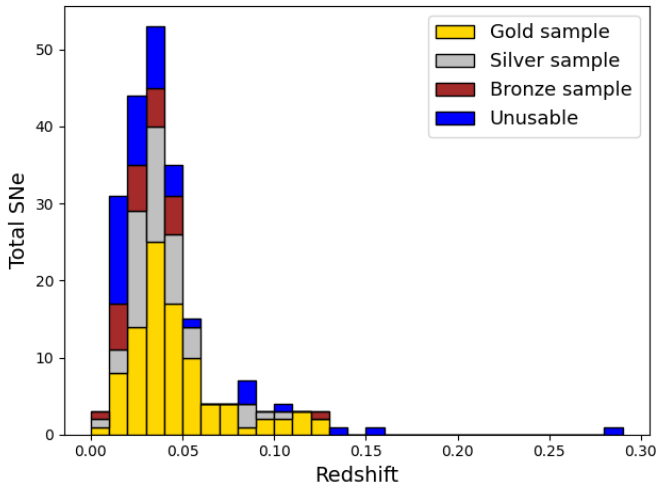

Figure 4. Distribution of redshifts in the sample. Redshifts of the gold sample are in yellow, silver in grey, bronze in brown, and unusable in blue. The majority of the redshifts in this sample are below 0.06.

$$e = \frac{a(x) + b(x)}{R_v} \cdot A(v) \tag{6}$$

Here $x = 1/\lambda$, where effective wavelengths were used for λ. Equations 4 and 5 are valid for $1.1\ \mu m^{-1} x < 3.3\ \mu m^{-1}$. As stated, the effective wavelengths were 6630 Å and 5182 Å, respectively. Thus respective x values are $x_o \approx 1.9\ \mu m^{-1}$ and $x_c \approx 1.5\ \mu m^{-1}$ which are within the limits. For total to selective extinction ratio R_V, standard Milky Way value was used: $R_V = \frac{A(V)}{E(B-V)} = 3.1$ as in the referenced paper.

3.3 Preparation of data

The goal was to find the distribution of rise-times in this sample, so to do that, the LCs had to be fitted. But before the actual fitting, a few steps had to be taken to filter and prepare. The data from ZTF needed more preparation than that of ATLAS; for this, ZTF provides instructions for each step [55].

Correction to rest-frame was performed for all data. This was done with equation 7, where t is the time in days since the explosion.

$$t_{restframe} = \frac{t_{obs}}{1+z} \tag{7}$$

The flux values from ATLAS were given in microjanskys and counts from ZTF. The ZTF values were, thus, converted to physical units, i.e. janskys, by using equation 8. In the equation, f_c is the flux in counts and zp stands for zero point. If an instrument observing an object registers one count per second, the object's magnitude is the system's zero point. The ZTF flux could have been converted to microjanskys as well, but since both would be converted into magnitudes later on anyway, it didn't matter which units were used in the intermediate steps.

With equation 9, flux values were converted to magnitudes. Here f is the flux, and for ZTF $f = f_{Jy}/3631$ to convert the flux from counts to janskys.

$$f_{Jy} = 10^{-0.4 \cdot \mathrm{zp}} \cdot f_c \cdot 3631 \tag{8}$$

$$m = -2.5 \cdot \log_{10}(f) \tag{9}$$

ZTF provides processing status codes in their files for each epoch. This *procstatus* column will show if the processing went successfully or if there were any problems, such as an epoch being impacted by bad pixels or an epoch not having a reference image within 5 arcseconds of the given coordinates. An epoch was included in the fit only if the processing went successfully. Most epochs were without errors, but some points or whole bands were excluded in a few cases.

The next step was to do a baseline correction for the ZTF data. Before the explosion and a significant time after the SN, the flux level from the SN should be relatively constant. Since this was differential photometry, this means that the flux level should be close to zero. The baseline, however, might not be at 0. For example, if there was flux from the SN itself, i.e. if the reference image had been taken after the explosion, it would contaminate the observations, and the baseline

would be negative. A positive baseline could also be because of a systematic error in the difference image generation or calibration [55].

The flux level was generally relatively flat before the explosion, and after the explosion, it returned to about the same level. Epochs from these periods were selected for the baseline.

To get a reliable baseline, at least 30 epochs should be included according to [55]. This was, however, not always possible. An epoch included information about the CCD camera field it was taken in. Each field has its own reference image, so the baseline for each field will be different. There were, in some instances, very few observations in a given field, but this also meant that there were only a few detections during the LC after the explosion, and thus, they didn't impact the LC greatly.

The baseline correction eliminated double curves in the LCs, which was a problem in some cases. For example, SN 2019etp, SN 2019qqw, SN 2019gqk and SN 2019hhh all had two almost identical curves, just horizontally separated. This was because two fields with different baselines displaced the two curves. With the baseline correction, they were combined into a single curve.

After the baseline correction, the next step was stacking. ATLAS and ZTF often image the same part of the sky multiple times a night, producing a large number of data points. All of these are not necessary for fitting the LC, and the figures are also a lot clearer if the points are instead stacked together.

ATLAS provides a code for stacking the data points [56], and this was used to stack the observations per one night. This was a separate code not incorporated into the final code used to produce the LCs, and instead, it was used in the data preparation phase. Thus, even though it can be used to stack multiple nights together, it was not done here, as stacking per one night produced the best results for most cases.

A code for stacking ZTF data was written for this project since ZTF does not provide a ready-made one. This code made it possible to modify how many nights of observations were stacked together. The observations were stacked every night for the most part, as they provided enough data points while still being easy to read. This was especially important for fast-evolving SNe, where stacking too many nights together would cause key information about the rise to be lost. If the SN was evolving slower and there were many observations, two to three nights were stacked together to improve the readability of LC. The goal of this thesis was not to study the variability of the LC, so it was possible to simplify the LC shape slightly. It is worth noting that as the division into subsamples included criteria involving the number of detections during the rise, this was determined by stacking the observations per one night for consistency's sake.

After stacking, the data points could be divided into detections and non-detections. In the case of ZTF, according to their documentation, detections were required to fulfil equation 10, where *forcediffimflux* is the differential flux in counts, *forcediffimfluxunc* its uncertainty in counts, and SNT is the signal-to-noise threshold. SNT = 3 was the value used. This criterion also determines that negative flux values always produce non-detections.

$$\text{forcediffimflux}/\text{forcediffimfluxunc} > \text{SNT} \tag{10}$$

As explained in Section 2.1, a visual inspection was needed even after this criterion as some data points assigned as detections were unrealistic. Such false detections were plotted separately and marked with crosses. This way, they would not affect the final fit of the LC, but they were not completely discarded.

ATLAS detections were required to fulfil equation 11 [48], where $m_{3\sigma}$ is the data point converted into magnitude space, and duJy is the error in flux (microjanskys). Negative flux values were also assigned as non-detections. This equation was used for both ATLAS bands.

$$m_{3\sigma} > -2.5 \cdot \log_{10}(3 \cdot \text{duJy}) + 23.9 \tag{11}$$

Uncertainties (unc) of the ZTF detections were calculated using equation 12 [55] to have it also in janskys instead of counts. Here $\frac{2.5}{\ln(10)} \approx 1.0857$ is a correction term between uncertainty in flux and same uncertainty in magnitudes.

$$\text{unc} = 10^{-0.4 \cdot \text{zp}} \cdot 1.0857 \cdot \text{forcediffimfluxunc} \cdot 3631 \tag{12}$$

ZTF non-detections (non-det) were plotted as 5σ upper limits. In apparent magnitudes, this is achieved by using equation 13, where signal-to-noise ratio or SNU = 5.

$$\text{non-det} = -2.5 \cdot \log_{10}(\text{SNU} \cdot \text{forcediffimfluxunc}/3631) \tag{13}$$

Finally, equation 14 was used to go from apparent magnitudes to absolute magnitudes. Here, M is the absolute magnitude, m is the apparent magnitude, DM is the distance modulus and A is the extinction.

$$M = m - \text{DM} - \text{A} \tag{14}$$

Figure 5 shows different data preparation steps. Type Ib SN 2019agx is used as an example. The upper left corner is the raw data before any adjustments with only ZTF bands. The upper right corner contains the same data after converting from counts to microjanskys, so both ATLAS and ZTF data are in the same units. Here, baseline correction for ZTF bands was also done. The plot is in the lower left corner after stacking. Finally, in the lower right corner, the data were converted into apparent and then absolute magnitudes, extinction correction was performed, and the fit of the LC was plotted as well. Different bands were shifted vertically to avoid overlapping, as noted in the legend. ATLAS non-detections were marked as squares for clarity and other symbols as circles. The LC fit using the Gaussian process (see discussion in Section 3.4) is the solid line, and the uncertainty of the fit is the shaded area.

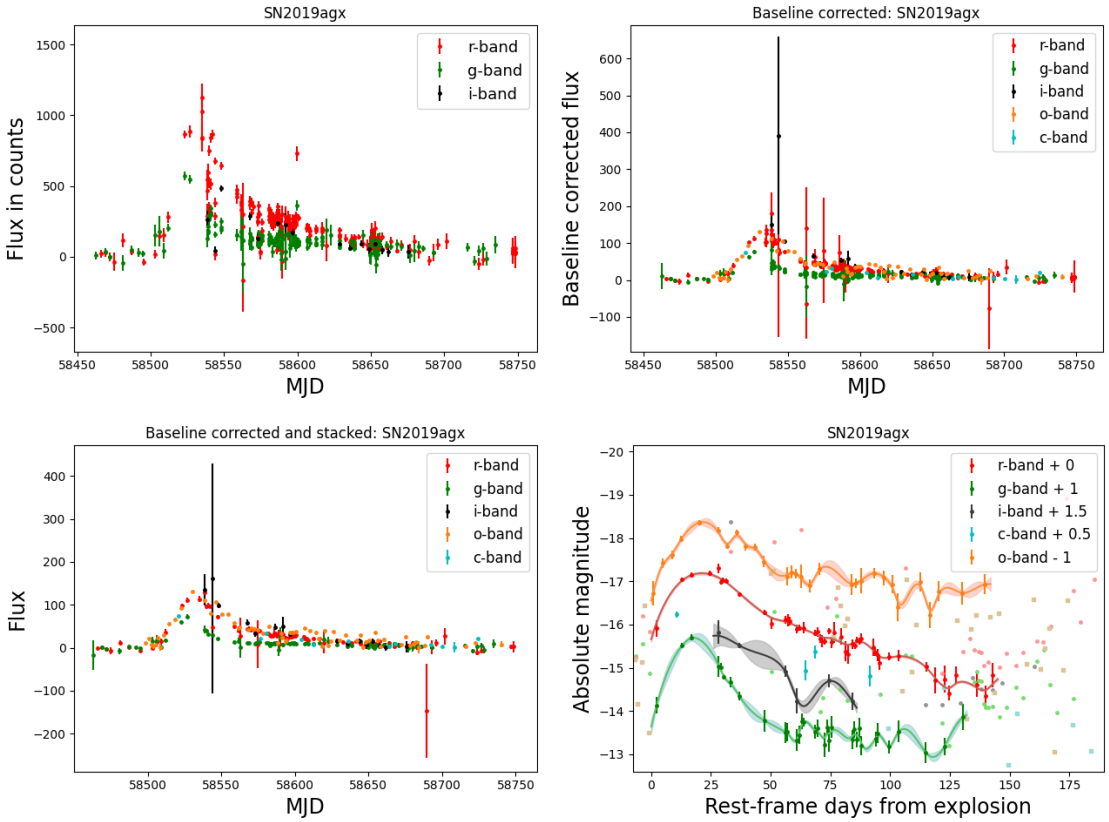

Figure 5. Different phases of preparing data, where type Ib SN 2019agx is used as an example. Top left: observations from ZTF before any preparation. Top right: ZTF data has been converted to microjanskys and baseline corrected. ATLAS data is also presented. Bottom left: both ZTF and ATLAS data have been stacked with binning for 24 hours. Bottom right: observations have been divided into detections and non-detections, data has been converted to magnitude space and to absolute magnitudes, and extinction correction has been performed (and different bands have been shifted vertically for clarity). The LCs have been fitted with Gaussia process (see section 3.4).

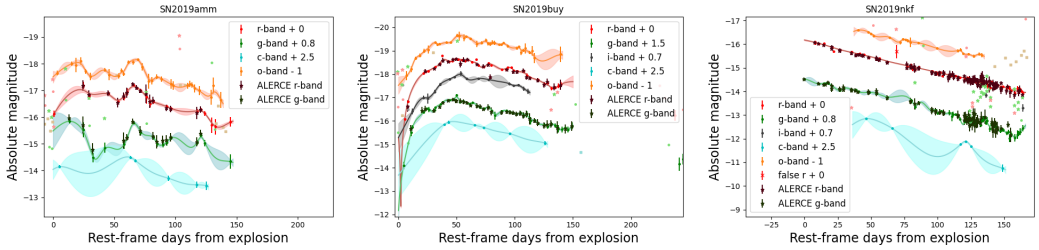

Figure 6. Comparison between obtained LCs and corresponding data from ALeRCE that is marked with stars. Both prepared data and data from ALeRCE are moved vertically equally for clarity. Left: SN 2019amm. Middle: SN 2019buy. Right: SN 2019nkf. As seen in all panels, the data from ALeRCE matches the prepared LCs very well.

To ensure these preparations were successful, the final curves were compared to data from Automatic Learning for the Rapid Classification of Events (ALeRCE)[7]. ALeRCE is a broker, processing the alert stream from ZTF. Due to time constraints, every SN could not be compared, but a few were selected, and they are shown in Figure 6. SN 2019amm (Ib), SN 2019buy (Ib) and SN 2019nkf (Ic) were used as examples. Photometry from ALeRCE is not forced photometry; fewer epochs are available on their website, and ALeRCE offers observations only in g- and r-bands. Therefore, a perfect match was not expected, but as seen in the figure, the magnitudes and LC shape are almost the same as the prepared data in this research.

3.4 Fitting the light curves

Once the data preparation was complete, it was time to fit the LCs. This was achieved with the Gaussian process, which is discussed in more detail in subsection 3.4.1.

As mentioned before, some bands had fewer epochs available. Trying to fit a LC based on only a few observations would not give reliable results, so no fitting was done if there were less than four detections. This was more common in i- and c-bands. The same would be applied if there were too large gaps between the few

[7]https://alerce.online/

detections, as this would not make for a reliable LC. In either case, detections and non-detections were still plotted in the figure.

To determine the peak of the LC, the smallest magnitude (most negative absolute magnitude) along the fit was taken. Multiple SNe, such as SN 2019hgy and SN 2019vkl, had double peaks in at least one band. In these cases, the higher and generally latter peak was taken as the main one for consistency. There were also multiple SNe with plateaus. In these cases, the approximate starting point of the plateau - or, in other words, the ending point of the rise - was defined as the peak.

Finally, after fitting the LC and defining the peak, each SN's rise-time and peak magnitude were obtained for further analysis.

3.4.1 Gaussian process

Gaussian process is the method chosen for this study to fit LCs. Python package GEORGE [57] was used in this study, but different implementations of the Gaussian process exist. The specific code used was based on the code used in [58][8].

For example, Stevance and Lee [59] give a good introduction to Gaussian processes. In it the idea is to fit a curve based on data points. The shape of the curve is not known in advance so it is approximated using a multivariate Gaussian distribution. Gaussian process uses machine learning to train a model based on the data and chosen covariance kernel. In this case the data are the photometric observations. The kernel is a function that shapes the characteristics of the curve. In the case of fitting a SN LC the curve isn't going to be periodic, and it might be important that the fit can accommodate sharp changes with a steeply rising LC. Therefore, the choice of the covariance kernel is important.

Since the fit produced by a Gaussian process model is only made to match the data points, it is not based on any physical model. Or in other words a physical

[8]https://github.com/cinserra/Gaussian-Processes-GP-/tree/master

model is not required. Additionally, Gaussian process provided uncertainties to the data points, inferred by the model, making it a very useful tool.

The most common kernel used in this thesis was Matèrn-3/2. As the reference states, it is good at fitting the rise since it allows for sharper changes in the LC but can cause overfitting in the tail. As the rise was the most important feature of the LC, this kernel was suitable for the majority of the SNe. Matèrn-3/2 is also aperiodic. A similar kernel is Matèrn-5/2, which is slightly smoother than the previous one, making it more appropriate for slower evolving LCs. A Matèrn kernel is defined by, among other variables, a positive value ν, which determines how many times the kernel is differentiable. In case of Matèrn-3/2 kernel $\nu = \frac{3}{2}$ and for Matèrn-5/2 $\nu = \frac{5}{2}$ [60].

More rarely squared exponential kernel, also known as radial basis function, was used. It was usually the smoothest of the options, so it would smooth out most of the undulations but might not represent a sharp rise very well. In cases of long, slow rises and many observations, this kernel was the best choice as it didn't overfit the small changes during the rise.

In addition to using single kernels, they can be combined. This is called kernel engineering. However, beyond testing this was not utilised, as testing different combinations takes a significant amount of time.

In addition to smoothness, the choice of kernel affected the rise-time and peak magnitude obtained from the LC. In most cases, the change in rise-time was in the order of minutes to hours. However, the rise-times obtained in this study are affected more by the uncertainty in estimating explosion epochs, which is in the order of days. Thus, the results are not highly dependent on the kernel choice. A change in the kernel could impact the rise-time a few days at most, but the difference being tens of days was very rare, and in these cases, the fit was significantly better with one of the kernels compared to others. The change in peak magnitude was also

not highly significant when comparing different kernels.

Different bands were fitted separately because they have different amounts of data and can evolve differently, i.e., they don't always have the same shape.

The kernel was chosen based on a visual inspection. Stevance and Lee state that the least squares method would not be useful in determining the best fit, as the most overfitting kernel would be favoured. A mathematical metric for a good or a bad fit would have to have some margin for over- and underfitting based on the underlying physics.

The Gaussian process is not a perfect method for fitting LCs, though it is relatively easy and fast to use. It can be prone to overfitting, and as stated before, the rise of the LC was the main focus of this study. Therefore, there would usually be overfitting in the tail, especially when fitting a sharp rise. This would be visible as undulations that likely are not real. To smooth these undulations, the rise would also have to be smoothed, leading to underfitting. As this was out of the scope of this thesis, it will have to remain as just a note for the future.

4 Results and discussion

4.1 Rise-times

The distribution of rise-times of every SN type in this sample is presented in Figure 7. The figure is divided into three panels displaying gold, silver and bronze samples from top to bottom. Different bands are presented in subplots in each of the panels. Different SN types are marked with different colours, as shown in the legend. As seen in the figure, the gold sample includes most of the complete sample, and the bronze sample has the smallest number of SNe, as it has only types Ib, II and IIn. Similarly, i- and c-bands have the smallest number of SNe.

In the gold sample, the majority of rise-times are towards the shorter end, which

Table 2. Mean rise-times in days of Ib SNe. The number of SNe used in each mean calculation is in parentheses below the mean value.

	g-band	r-band	i-band	c-band	o-band
Gold sample	18 ±4	21 ±4	16 ±3	15 ±3	22 ±6
	(7)	(6)	(1)	(1)	(7)
Silver sample	12 ±0.8	14 ±11	22 ±0.5	-	10 ±4
	(2)	(2)	(1)	(0)	(1)
Bronze sample	16 ±8	20 ±6	-	9	17 ±7
	(2)	(2)	(0)	(1)	(3)

is best seen in g-, r—and o-bands that have the largest number of SNe. Most rise-times are below 35 days. Rise-times also tend to be longer in gold samples, likely because of criterion bias. This is most visible in types Ib, II, IIb, and IIn. One reason for this could be the larger number of SNe in the gold sample as well.

SNe IIn have the longest rise-times, though there is quite a lot of variation among this subclass. The shortest rise-times among SNe IIn are about 10 days, depending on the band, and the longest is more than 80 days. SNe II also display quite a bit of variation, though this is also the type with the largest number of SNe in this sample.

To get a more detailed picture of each SN type, their rise-time distributions are presented and discussed. When more than one SN was included in the calculation, uncertainties were calculated as the standard deviation of rise-times. With only one SN, its uncertainty from the explosion epoch estimation was used. For more discussion about the uncertainties, see the appendix.

SNe Ib: Mean rise-times of type Ib SNe in each band are presented in Table 2, and the distribution of SNe Ib rise-times are in Figure 8. Each band is shown in a different subplot in the figure: the gold sample is yellow, the silver sample is grey, and the bronze is brown. All bronze sample values were lower limits, meaning they

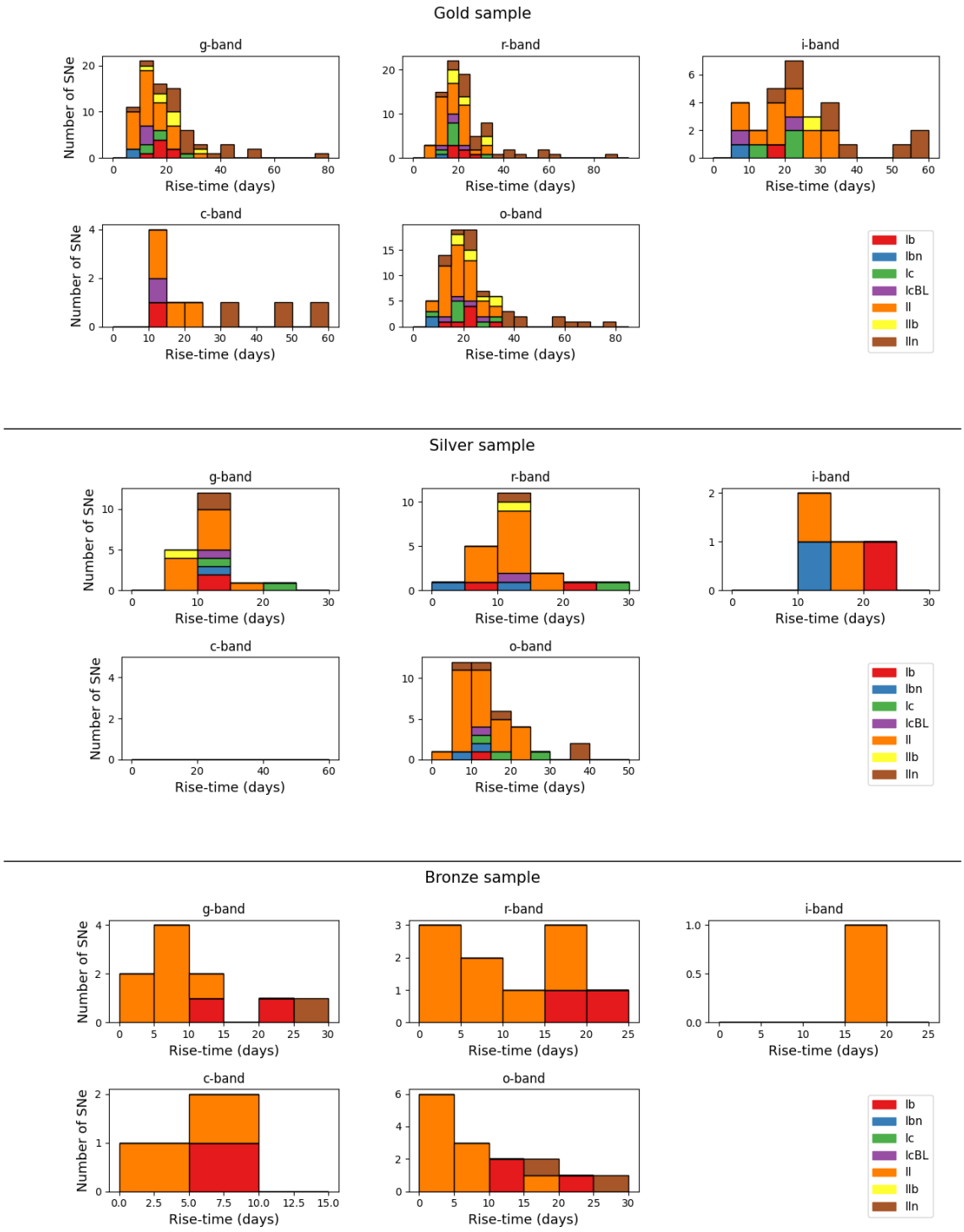

Figure 7. Rise-times of all SN types in the gold (top), silver (middle) and bronze (bottom) subsamples. Different bands are divided into subplots, and different types are colour-coded, as shown in the legends. The x-axis is the rise-time in days, and the y-axis shows the number of SNe in each bin. The width of each bin is 5 days.

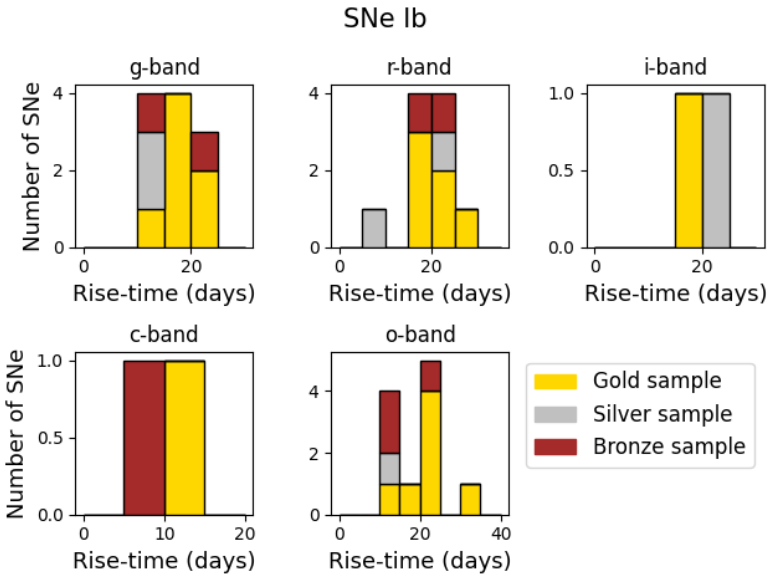

Figure 8. Rise-times of type Ib SNe. Different bands are divided into subplots, and different subsamples are marked with gold, silver and bronze colours. The width of each bin is 5 days.

had no deep non-detection within 20 days, so the first detection was used as the explosion epoch instead. This means that no uncertainty could be obtained from the explosion epoch estimation, and there is no uncertainty in the c-band.

In this sample, the previously mentioned rule of longer rise-times for redder bands seems to hold. The exception of the gold sample i-band, which is shorter than the other bands, is likely because only one SN belongs in that subsample and band. Additionally, there was one SN with enough observations in the i-band, but this SN 2019buy belongs to the peculiar subsample, so it is not included here and is discussed more in subsection 4.4.

Taddia et al. [17] investigated the rise-times of nine SNe Ib and found a mean rise-time of 21.3 $\pm$ 0.4 days in r/R-band, which is close to ZTF r-band. This is in good agreement with the gold sample r-band results of this study and relatively close to the bronze sample. Silver sample rise-times are significantly shorter, which can be because the criteria do not bias the SNe as much towards longer rise-times. All bronze sample SNe Ib were lower limits, so their mean rise-times are likely higher.

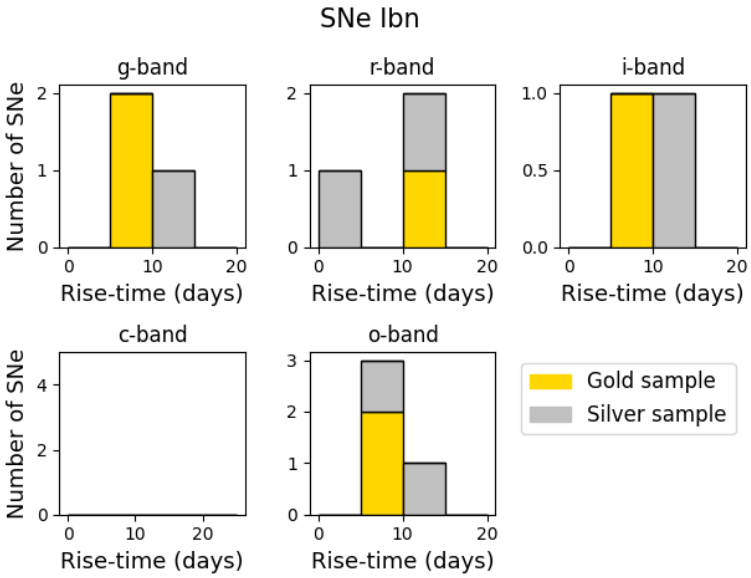

Figure 9. Rise-times of type Ibn SNe. Different bands are divided into subplots, and different subsamples are marked with gold, silver and bronze colours. The width of each bin is 5 days.

SNe Ibn: Mean rise-times of type Ibn SNe in each band are presented in Table 3, and the distribution of Ibn rise-times are in Figure 9. There are too few SNe to make very concrete claims, but based on the four SNe Ibn in this sample, their rise-times seem to be ≤ 14 days. This would make them quicker to evolve than type Ib SNe.

SNe Ibn, being fast-evolving, agrees with Hosseinzadeh et al. [25]. Similar or shorter rise-times were found here as Hosseinzadeh et al., who investigated 22 SNe Ibn, though their sample had more diversity than can be found in this limited sample. These rise-times varied from 1.6 ± 0.9 days to 16.9 ± 1.9 days. They also found that SN Ibn LCs are more homogeneous than those of SNe IIn, even though both are interacting types. The LCs of SNe Ibn in this sample are also relatively uniform.

SNe Ic: Mean rise-times of type Ic SNe in each band are presented in Table 4, and the distribution of Ic rise-times are in Figure 10.

Table 3. Mean rise-times in days of Ibn SNe. The number of SNe used in each mean calculation is in parentheses below the mean value.

	g-band	r-band	i-band	c-band	o-band
Gold sample	9 ±2	11 ±1	9 ±2	-	9 ±0.5
	(2)	(1)	(1)	(0)	(2)
Silver sample	14 ±4	9 ±6	14 ±4	-	9 ±5
	(1)	(2)	(1)	(0)	(2)
Bronze sample	-	-	-	-	-
	(0)	(0)	(0)	(0)	(0)

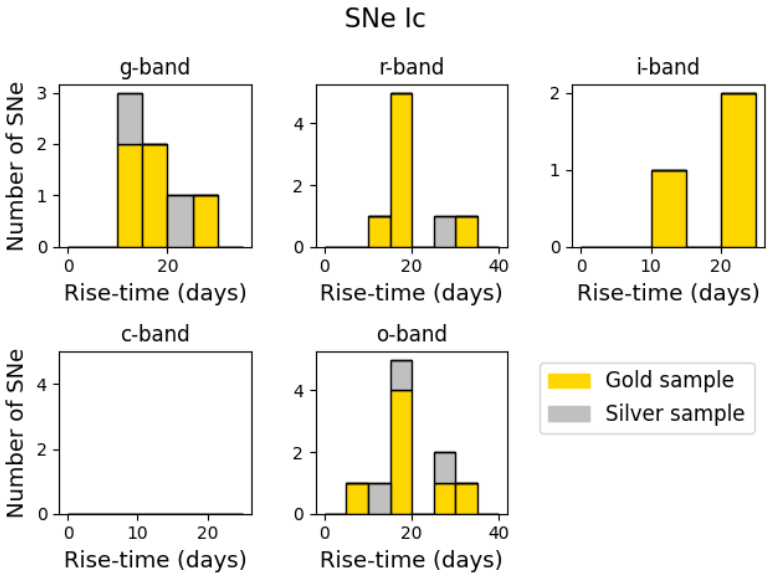

Figure 10. Rise-times of type Ic SNe. Different bands are divided into subplots, and different subsamples are marked with gold, silver and bronze colours. The width of each bin is 5 days.

Table 4. Mean rise-times in days of Ic SNe. The number of SNe used in each mean calculation is in parentheses below the mean value.

	g-band	r-band	i-band	c-band	o-band
Gold sample	17 ±7	19 ±6	19 ±4	-	19 ±8
	(5)	(7)	(3)	(0)	(7)
Silver sample	18 ±5	28 ±9	-	-	19 ±7
	(2)	(1)	(0)	(0)	(3)
Bronze sample	-	-	-	-	-
	(0)	(0)	(0)	(0)	(0)

There was a significant dispersion in the rise-times of Ic SNe in this sample, ranging from less than 10 days to more than 40 days. The longest rise-times in this sample belong to double-peaked SNe SN 2019dwa and SN 2019cad of the peculiar sample. They were not included in the analysis here and are discussed more in Section 4.4.

Taddia et al. [17] found a mean rise-time for six type Ic SNe to be 11.5 ± 0.5 days in r/R-band, which is significantly shorter than the mean obtained here when comparing with r-band 19 days in gold sample (and even more so with 28 days in silver sample). The number of SNe in the sample of this thesis is twice as large, so it may give a more accurate representation of the rise-time length. On the other hand, at least in the gold sample, there is likely a bias towards longer rise-times.

SNe Ic-BL: Mean rise-times of type Ic-BL SNe in each band are presented in Table 5, and the distribution of Ic-BL rise-times are in Figure 11. The number of Ic-BL SNe in this sample is not very large as it consists only of six SNe.

Taddia et al. [17] found the mean rise-time of five Ic-BL SNe to be 14.7 ± 0.2 days in r/R-band, and then in another study, Taddia et al. [61] studied 34 type Ic-BL SNe and found their mean rise-time to be 15 ± 6 days. This is significantly

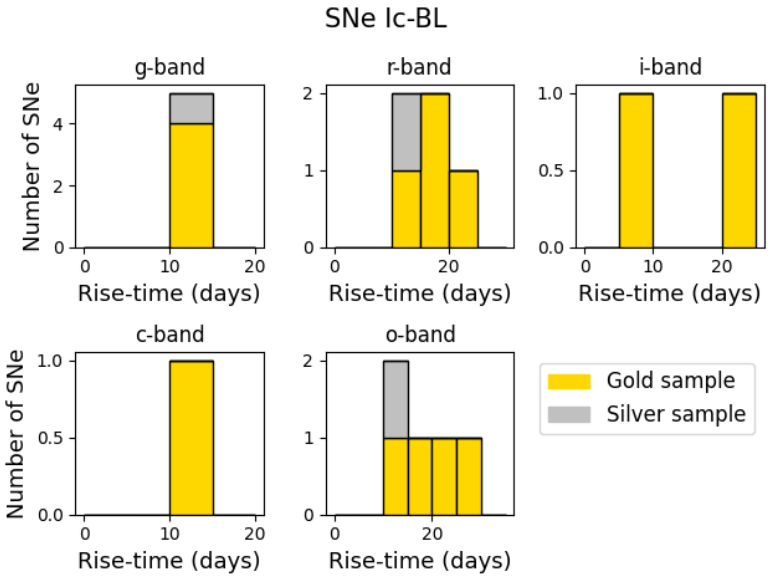

Figure 11. Rise-times of type Ic-BL SNe. Different bands are divided into subplots, and different subsamples are marked with gold, silver and bronze colours. The width of each bin is 5 days.

Table 5. Mean rise-times in days of Ic-BL SNe. The number of SNe used in each mean calculation is in parentheses below the mean value.

	g-band	r-band	i-band	c-band	o-band
Gold sample	12 ±2	19 ±5	15 ±8	14 ±3	19 ±8
	(4)	(4)	(2)	(1)	(4)
Silver sample	12 ±3	15 ±3	-	-	12 ±3
	(1)	(1)	(0)	(0)	(1)
Bronze sample	-	-	-	-	-
	(0)	(0)	(0)	(0)	(0)

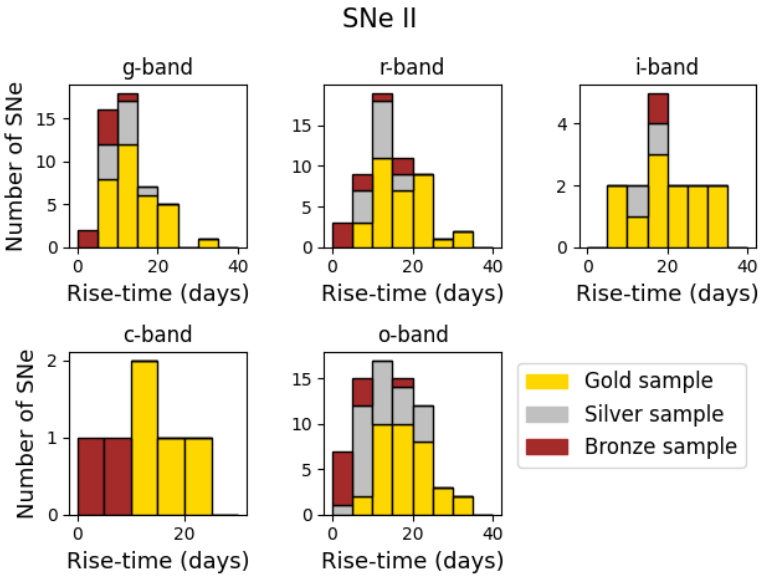

Figure 12. Rise-times of type II SNe. Different bands are divided into subplots, and different subsamples are marked with gold, silver and bronze colours. The width of each bin is 5 days.

shorter than the rise-time in the gold sample. However, the mean rise-time in the r-band silver sample is much closer to their reported value, which could be because of the already mentioned bias.

In [17], they also found that in order of shortest to longest, rise-times are SNe Ic-BL, Ic, Ib and IIb. Though there doesn't seem to be such a precise order between SNe Ib and IIb in the sample of this thesis, the rise-times of SNe Ib are generally longer than those of SNe Ic that are further longer than the rise-times of Ic-BL SNe, thus agreeing with Taddia et al. [17].

SNe II: Mean rise-times of type II SNe in each band are presented in Table 6, and the distribution of type II SN rise-times are in Figure 12. As seen from the table, rise-times grow longer with redder bands, and most rise-times are below 30 days, although this is a high limit for type II SNe. SN 2019bjr, SN 2019vrl and SN 2019zeb are notable exceptions discussed in more detail in section 4.4 and not included here.

Table 6. Mean rise-times in days of II SNe. The number of SNe used in each mean calculation is in parentheses below the mean value.

	g-band	r-band	i-band	c-band	o-band
Gold sample	14 ±6	17 ±7	20 ±9	15 ±6	18 ±7
	(32)	(33)	(12)	(4)	(35)
Silver sample	11 ±5	12 ±5	15 ±2	-	12 ±6
	(10)	(13)	(2)	(0)	(26)
Bronze sample	6 ±4	9 ±7	16 ±7	6 ±5	6 ±5
	(7)	(8)	(1)	(2)	(10)

Table 7. Rise-times from González-Gaitán et al. [18] for comparison. Presented are median values of type II SNe of different subsamples and in different wavelengths.

λ_{eff}	SDSS-SN golden	SDSS-SN silver	SNLS golden	SNLS silver
4700 Å	-	-	$12.0^{+1.6}_{-5.8}$	$11.5^{+4.8}_{-4.0}$
5600 Å	$7.9^{+3.6}_{-2.9}$	$8.3^{+4.0}_{-2.8}$	$12.6^{+4.1}_{-4.1}$	$12.3^{+6.8}_{-3.5}$
6700 Å	$8.1^{+3.4}_{-1.6}$	$9.7^{+4.0}_{-3.3}$	$14.6^{+8.9}_{-5.5}$	$14.7^{+9.0}_{-5.6}$
8200 Å	$10.1^{+3.6}_{-2.3}$	$11.0^{+5.8}_{-3.5}$	-	-

González-Gaitán et al. [18] investigated 223 type II SNe and their photometric properties. They have separate samples for SDSS-SN (Sloan Digital Sky Survey) and SNLS (SuperNova Legacy Survey) data with 48 and 38 SNe in their golden samples, respectively. They also have a silver sample, but unlike in this study, their silver samples include their golden samples, and they have 131 and 92 SNe, respectively. These results, insofar as relevant in this comparison, are presented in table 7. The value used was their $t_{\text{rise}}^{\text{end}}$, as it matches better with how rise-times were obtained in this study.

The first relevant effective wavelength is 4700 Å, which is close to the ZTF g-band. Results only include SNLS, which doesn't have as good a cadence as SDSS-SN. Both gold and silver sample values of this thesis are in quite good agreement

with their golden and especially silver sample values. The bronze sample has a significantly shorter rise-time mean than other subsamples of either study.

In addition to González-Gaitán et al., also Pessi et al. [62] investigated 73 type II SNe. They found the weighted average rise-time in the B-band to be 8.3±2.0 days. This is slightly shorter than the 14 days found here but closer to silver and bronze sample values. This could be explained by the fact that the effective wavelength of the B-band is slightly shorter than that of the g-band. Additionally, the criteria for silver and especially gold subsamples are biased towards longer rise-times.

González-Gaitán et al. report median rise-times at 5600 Å, which is closest to ATLAS c-band. However, the difference between bands is more significant: 420 Å. The gold sample of this thesis is slightly longer but within their golden SNLS sample error margins, and the bronze sample is shorter but within their golden SDSS-SN sample error margins. There were no SNe in the sample of this thesis that belonged to the silver subsample and had enough epochs in the c-band to constrain a rise. In fact, despite type II SNe making up the majority of this sample, there were only seven type II SNe in the whole sample of this thesis that had a c-band rise.

Pessi et al. report the weighted average rise-time of type II SNe in V-band to be 12.8±2.4 days. This is closest to the c-band, though the V-band effective wavelength is longer. Nevertheless, this is shorter than that of the gold sample but longer than the bronze sample's median rise-time. Again, one possible explanation is the bias in the gold subsample.

The effective wavelength 6700 Å from González-Gaitán et al. is closest to ATLAS o-band and relatively close to ZTF r-band. SNLS median rise-times for both golden and silver samples have large uncertainties and agree with both r- and o-band gold and silver means of this thesis. However, SDSS-SN has better constrained median rise-times that only agree with r-band silver and bronze mean values and o-band silver mean rise-time. Thus, even though there is some agreement, the results of this

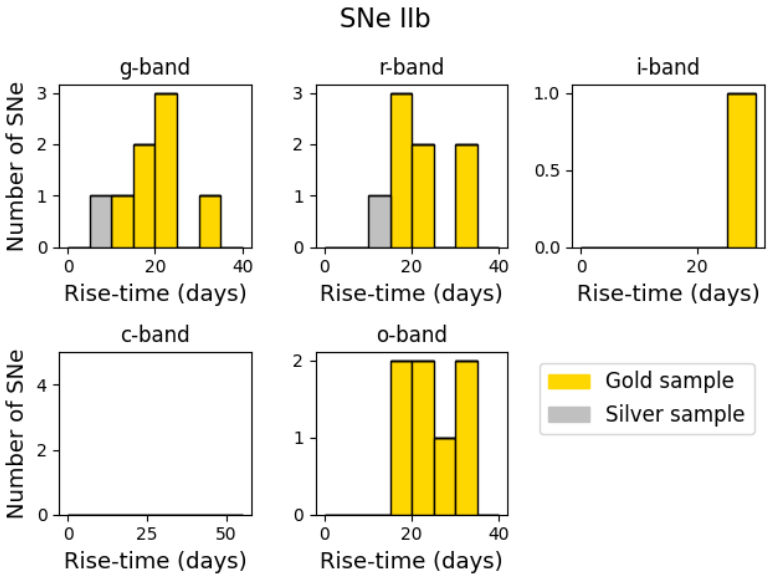

Figure 13. Rise-times of type IIb SNe. Different bands are divided into subplots, and different subsamples are marked with gold, silver and bronze colours. The width of each bin is 5 days.

study tend to have longer rise-times than González-Gaitán et al. report. It is quite clear that the golden sample tends to have longer rise-times, which could at least partially be due to the selection criterion. Since González-Gaitán et al. reported shorter rise-times, they agree better with silver and bronze samples where the bias towards longer rise-times isn't as strong.

Pessi et al. report a weighted average rise-time in the r-band of 16.0±3.6 days. This agrees well with the 17 days found in the gold subsample in the r-band.

ZTF i-band is closest to the 8200 Å effective wavelength from González-Gaitán et al., but the difference is about 370 Å. In this thesis, the mean of the gold sample is 20 days, which is approximately double that of González-Gaitán et al. Both silver and bronze sample medians are closer to SDSS-SN median values but are still noticeably longer.

SNe IIb: Mean rise-times of type IIb SNe in each band are presented in table 8, and the distribution of IIb rise-times are in figure 13.

Table 8. Mean rise-times in days of IIb SNe. The number of SNe used in each mean calculation is in parentheses below the mean value.

	g-band	r-band	i-band	c-band	o-band
Gold sample	21 ±6	23 ±7	25 ±4	-	24 ±6
	(7)	(7)	(1)	(0)	(7)
Silver sample	10 ±2	13 ±2	-	-	-
	(1)	(1)	(0)	(0)	(0)
Bronze sample	-	-	-	-	-
	(0)	(0)	(0)	(0)	(0)

Taddia et al. [17] found the mean rise-time for type IIb SNe to be 22.9 ± 0.8 days in r/R-band. The mean rise-time of the gold sample in the r-band in this thesis is 23 days, which agrees with Taddia et al.

Pessi et al. [62] investigated 22 type IIb SNe and found weighted average rise-times of 19.0±1.8 days in B-band (closest to g-band) and 21.3±2.1 days in r-band. Both g- and r-band rise-times found in this thesis are within those B- and r-band values, respectively, though both values in this thesis are somewhat longer. Since no c-band values are found here, they cannot be compared to the V-band (closest to the c-band in terms of wavelength) values reported by Pessi et al.

Pessi et al. also note that the difference in rise-times between bands is small. Here, the mean values are relatively similar, but there is some variation. In particular, the i-band is longer, but there is only one SN with enough data points in the i-band to constrain a rise-time. The rise-times found in the silver sample are much shorter than those in the gold sample, likely due to the gold sample bias.

SNe IIn: Mean rise-times of type IIn SNe in each band are presented in Table 9, and the distribution of IIn rise-times are in Figure 14. From the figure, it is clear that there is a wide range of rise-times among SNe IIn, which has also been stated

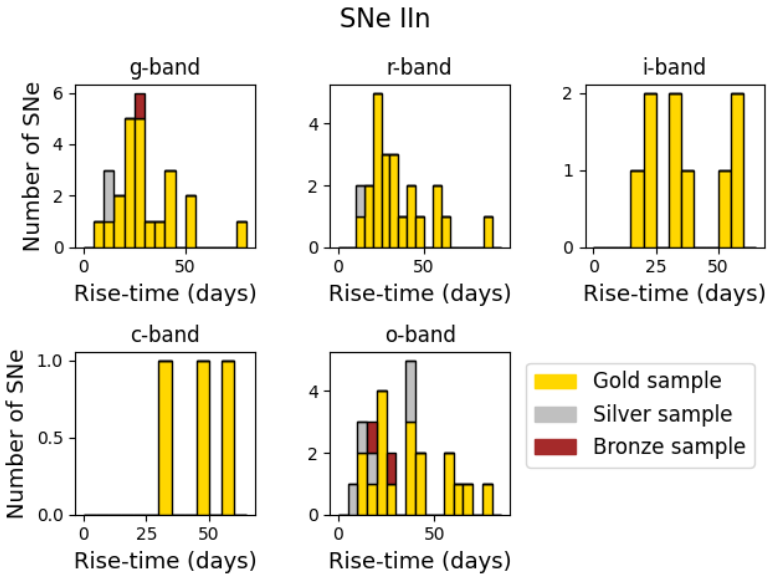

Figure 14. Rise-times of type IIn SNe. Different bands are divided into subplots, and different subsamples are marked with gold, silver and bronze colours. The width of each bin is 5 days.

Table 9. Mean rise-times in days of IIn SNe. The number of SNe used in each mean calculation is in parentheses below the mean value.

	g-band	r-band	i-band	c-band	o-band
Gold sample	31 ±16	35 ±19	37 ±17	46 ±15	38 ±20
	(22)	(22)	(9)	(3)	(18)
Silver sample	13 ±0.9	12 ±0.4	-	-	22 ±14
	(2)	(1)	(0)	(0)	(5)
Bronze sample	25	-	-	-	22 ±5
	(1)	(0)	(0)	(0)	(2)

by Nyholm et al. [63]. This is also reflected in the large uncertainties. Again, all bronze sample values were lower limits, so no uncertainty could be obtained from the explosion epoch estimation, and there is no uncertainty in g-band, where there is only one SN.

The median rise-time is quite high, especially in the c-band, but only three SNe have enough epochs in the c-band to estimate a rise-time, so this number is hardly generally representative.

Nyholm et al. [63] found two samples of rise-times in their sample of 32 type IIn SNe: 20 ± 6 days and 50 ± 11 days. These were mainly imaged in R/r-band, but in four cases, data were unavailable, so they used g-band instead. In this sample, no such clear bimodal distribution can be seen. The mean value in the silver sample r-band is shorter than this, and the gold sample sits between the shorter and longer rise-time groups, likely because the sample of this thesis formed a more uniform distribution. Considering that the values of Nyholm et al. are not exclusively R/r-band values, they are not perfectly comparable.

In some cases, Active Galactic Nuclei (AGN) can be misclassified as type IIn SNe or vice versa. To rule out this possible misclassification in at least some cases, the locations of the SNe in their host galaxies were checked. Of the 30 SNe in this sample (not including the unusable SNe), 3 were located in the middle of their host galaxy, 21 were not, and in 6 cases, it was unclear because the host galaxy was too faint. Therefore, at least 21 of the SNe IIn in this sample could not have been AGNs, but with the rest, further checks, such as investigating their spectra and seeing if there has been any previous activity, could be made to be certain. This was not done here due to time constraints.

4.2 Rise-time dependence on band

This section explores the difference in rise-time lengths between different bands. The ZTF g- and r-bands were chosen since many SNe have enough data points in these bands. In Figure 15, the length of rise-time in r minus the length of rise-time in g (in days) are presented for each SN subtype, and different subsamples are marked with colours. The peculiar subsample is not included in this figure.

For the most part, the difference in rise-time lengths is clearly less than 10 days, and the rise-time is longer in the r-band. There are, however, a few cases where the difference is longer, or the g-band rise-time is longer than that of the r-band. The largest differences are in type II and IIn SNe. The latter especially has large differences, with the largest being about 21.4 and 23.7 days. Similarly, there were more SNe IIn that had a longer rise-time in the g-band.

All SNe, which had longer rise-times in g than r were checked. In the case of SN 2019ehk (Ib) there was a lack of points in g-band in the early phase. In r-band, two bumps in the LC can be seen, but the g-band peak occurs just before the second r-band bump. Therefore, it is entirely possible that the g-band main peak would have occurred earlier and the visible peak is simply a later occurring bump, making the g-band rise-time shorter. Without the missing data coverage, it is impossible to say for certain.

SN 2019fcb (Ibn) has only a few detections before and around the main peak. Therefore, the LC fit is hardly perfect. If one changes the kernel used in the fit, the already small difference in rise-time lengths becomes even smaller. Thus, this one as well could simply be due to the lack of data.

SN 2019bhq (II) has no detections during the rise, but it does have a good non-detection, making it part of the bronze sample. The first detections were used as the rise-time upper limit, and the r-band detection was observed before the g-band first detection. Thus, one can not really say if the g-band rise-time is actually longer

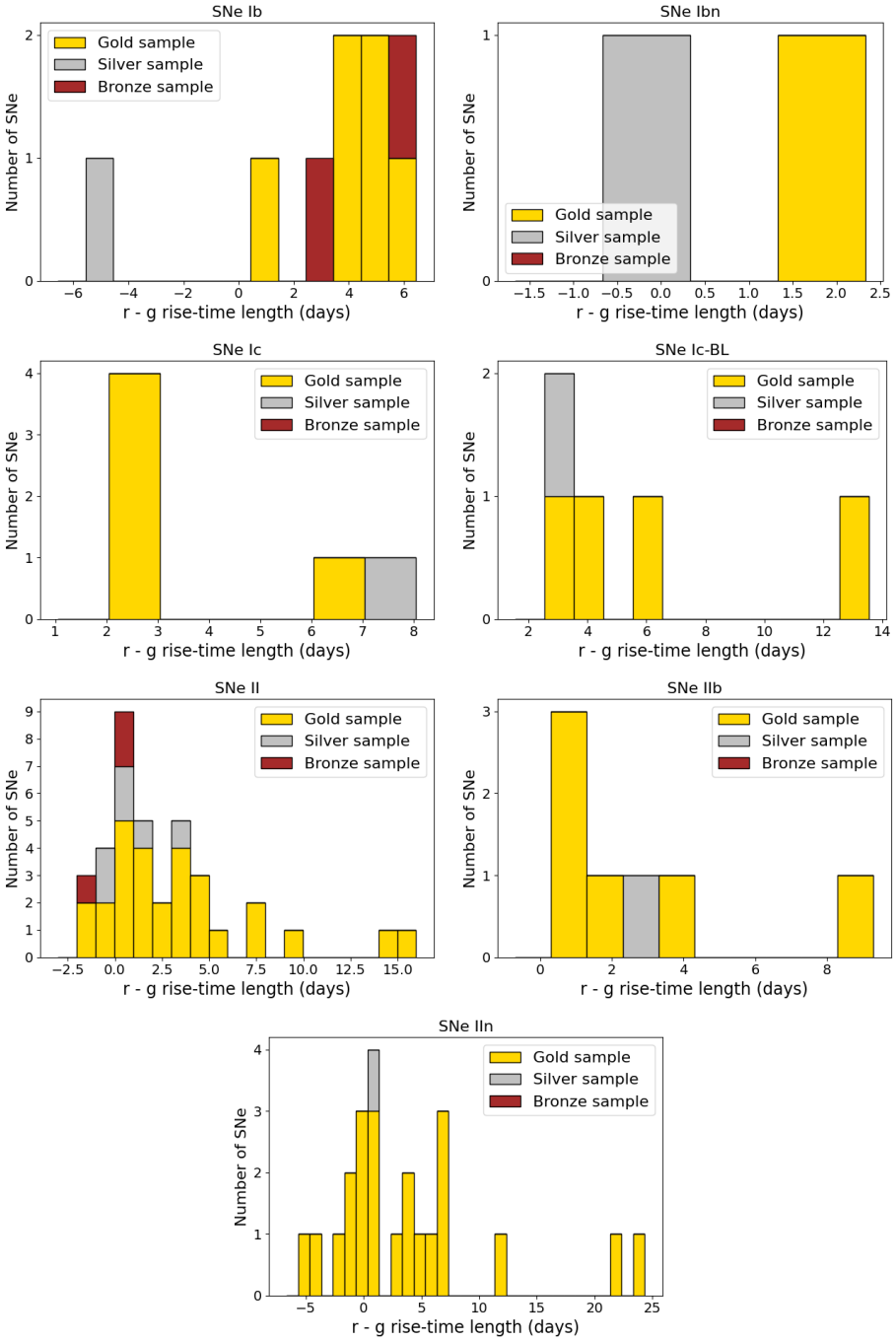

Figure 15. Difference in rise-time lengths between r- and g-bands (in days). Each SN type is presented in a different subplot, and subsamples are marked with gold, silver and bronze colours. The peculiar subsample is not included. The width of each bin is 1 day.

since no peak can be constrained.

With SN 2019eju (II) the difference is only 0.5 days and there is no clear lack of data. Therefore, it seems that in this case, the g-band rise-time is simply slightly longer. Similarly, with SN 2019qqw (II), the longer rise-time in the g-band looks real based on the data, which has no obvious gaps. SN 2019gcn (II) does not have quite as long a period of observations as the two previous ones, but with the data available, it also seems to have a longer rise-time in the g-band.

SN 2019gss (II) has only one detection in both r- and g-bands before the peak, but in the r-band, it is closer to the peak. Therefore, the peak is approximate. This difference in rise-time lengths could be real, but it could also be because of the uncertain peak time.

The LC of SN 2019xvo (II) in r-band plateaus, which again makes the time of the peak approximate, since the determination of the peak was done with only visual inspection. If more quantitative measures were used, such as defining the peak to be the point were change in the luminosity is less than some threshold, a more accurate time of peak could have been established. Nevertheless, the peak does seem to occur later in g-band.

SN 2019bxq (IIn) has some variability in its LC, though there are no big gaps in observations. Therefore, interpreting the LC is more difficult. Depending on which bump is considered the main peak, either the r- or g-band is longer. The highest bump was defined as the peak here, and with it, the g-band is somewhat longer.

SN 2019dde (IIn) also has two bumps, but in both, the g-band peak occurs slightly later, so the difference is likely real. Similarly, the rise-time length difference in SN 2019dvv (IIn), SN 2019krt (IIn), SN 2019qny (IIn), and SN 2019vkl (IIn) look like real ones, as they don't have any clear gaps in observations.

4.3 Peak magnitude versus rise-time

This section discusses the possible relation between peak absolute magnitude and rise-time. Figures 16 - 18 present peak magnitude versus rise-time. Each SN type is presented separately, and the type is at the top of each panel. At the bottom, all SNe of every type are plotted together. Since rise-time and peak magnitude vary depending on wavelength, all bands are plotted separately in each panel.

There are too few SNe Ibn to accurately describe a correlation. However, a possible correlation can be seen in type Ib SNe, where longer rise-times also mean higher peak magnitudes. The exception is in the c-band, where there are only two SNe, which is insufficient to establish a correlation or lack thereof.

It is worth noting that the lack of host extinction and possible errors in distance calculations affect peak mag and, therefore, the correlation.

We use the Pearson correlation to get a more quantitative measure of correlation. This test is used to estimate whether there is a linear correlation between two data sets. Pearson coefficient is given by equation 15, where μ_x is the mean of variable x and μ_y is the mean of variable y. Here x is the rise-time, and y is the peak absolute magnitude. Pearson coefficient always gives a result $\in$ [-1,1], where -1 means a perfect negative correlation, 0 means no correlation between the data sets, and 1 means a perfect positive correlation.

$$r = \frac{\Sigma(x - \mu_x)(y - \mu_y)}{\Sigma(x - \mu_x)^2 \Sigma(y - \mu_y)^2} \tag{15}$$

In addition to the Pearson coefficient, an important metric is also the p-value. It describes how likely a random sample would indicate a correlation as high as the calculated Pearson coefficient.

The coefficients and p-values for each SN type and for all SN types combined were calculated and are presented in Table 10. The SCIPY.STATS.PEARSONRfunction [64] was used in the calculation. The coefficients and p-values are calculated separately

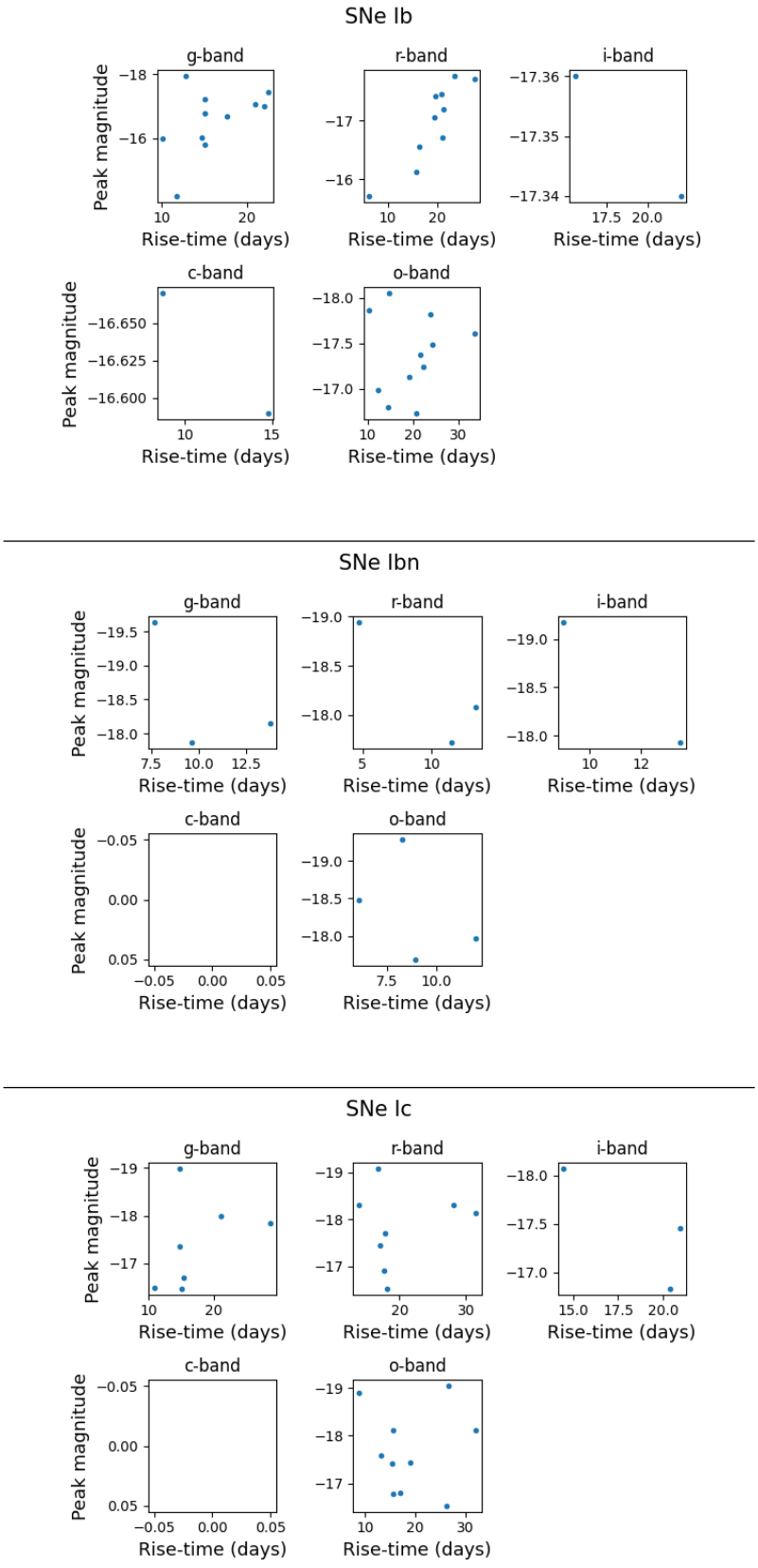

Figure 16. Peak absolute magnitude versus rise-time. Different bands are plotted in subplots. Top panel: type Ib SNe, middle panel: type Ibn SNe, bottom panel: type Ic SNe.

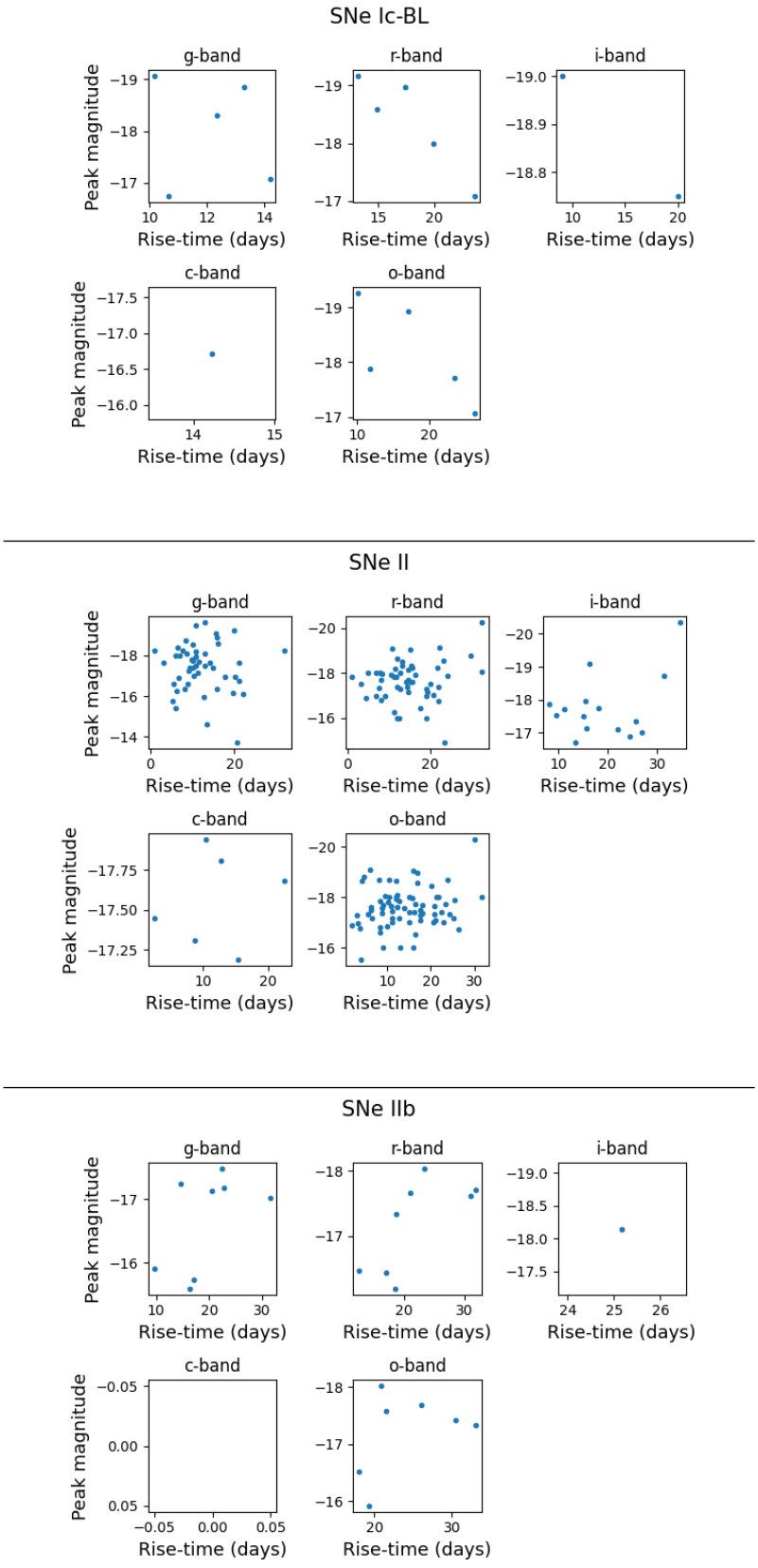

Figure 17. Peak absolute magnitude versus rise-time. Different bands are plotted in subplots. Top panel: type Ic-BL SNe, middle panel: type II SNe, bottom panel: type IIb SNe.

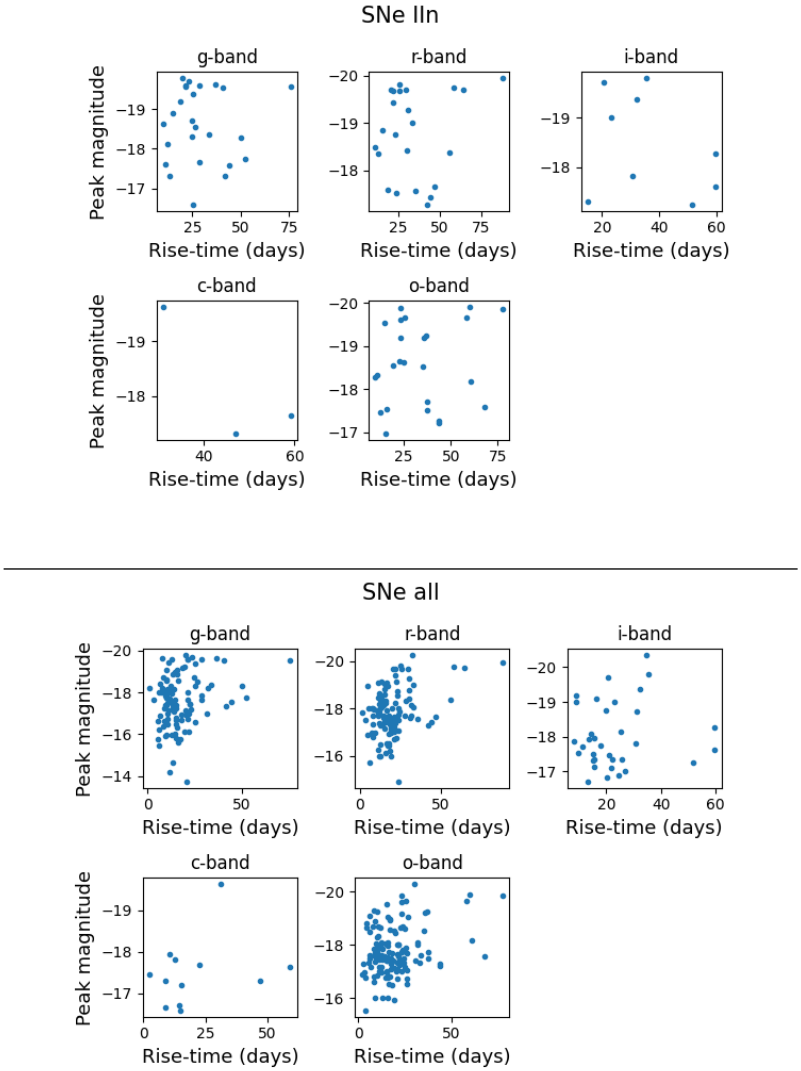

Figure 18. Peak absolute magnitude versus rise-time. Different bands are plotted in subplots. Top panel: type IIn SNe, bottom panel: all SNe of every type.

Table 10. Pearson coefficients/p-values of peak absolute magnitude versus rise-time for all SN types and all bands. Only those values are reported where more than three SNe are available for calculation. The peculiar subsample has not been included. Below each coefficient/p-value is the number of SNe used in the calculation. Moderate and higher correlations (coefficient <0.-40 or >0.40 and p-value $\leq$ 0.05) are highlighted in bold.

	g-band	r-band	i-band	c-band	o-band
Ib	-0.49/0.1 11	**-0.89/0.0005** 10	- -	- -	-0.09/0.8 11
Ibn	- -	- -	- -	- -	0.42/0.6 4
Ic	-0.38/0.4 7	-0.18/0.7 8	- -	- -	-0.005/0.9 10
Ic-BL	0.16/0.8 5	**0.92/0.03** 5	- -	- -	0.75/0.1 5
II	0.06/0.7 49	-0.17/0.2 54	-0.40/0.1 15	-0.15/0.8 6	-0.18/0.1 71
IIb	-0.53/0.2 8	**-0.70/0.05** 8	- -	- -	-0.40/0.4 7
IIn	-0.04/0.9 25	-0.15/0.5 23	0.33/0.4 9	- -	-0.16/0.5 25

for each band, and a result is given only if there are four or more SNe in the calculation.

These coefficients were interpreted similarly as in [65]. No significant correlation could be found if the value is -0.19 < coefficient < 0.19. A weak correlation would be ±0.20-0.39 (positive or negative correlation), a moderate correlation ±0.40-0.59, a strong correlation ±0.60-0.79 and a very strong correlation ±0.80-1. Additionally, the p-value must, of course, be taken into account as well, and a correlation was considered significant if the p-value$\leq$0.05. Most values indicate no significant

correlation with this criteria, but some exceptions exist. Interestingly, significant correlations were found only in r-band.

SNe Ib indicate moderate and very strong negative correlations in g- and r-bands, respectively. This is not found in o-band, though; nothing could be said about i- and c-bands due to the small number of SNe. Nevertheless, the correlation, especially in r-band, appears to be real.

In the r-band, a strong positive correlation is found among SNe Ic-BL, but again, this is not the case with other bands. Though the p-value is small enough in the r-band, the number of SNe is still small, and more robust conclusions could be drawn from a larger sample. Thus, even though this could indicate a correlation, it is not enough to say for certain.

Another strong negative correlation could be found in SNe IIb, though the p-value is just at the higher limit. Other calculated values don't indicate a significant correlation.

Gall et al. [66] investigated a sample of 20 type II SNe and found a slight correlation between peak magnitude and rise-time. No clear correlation is found among type II SNe of this sample, which is in agreement with Faran et al. [67], who investigated eight SNe II-P (that are included but don't necessarily make up the entire type II category in this thesis). They compared rise-time to the plateau luminosity and found no significant correlation. As the sample size of this study is larger than those of either mentioned studies, it is likely that type II SNe have no correlation between peak magnitude and rise-time.

SNe IIn are very versatile, and in this sample, there doesn't seem to be at least any linear correlation between rise-time and peak absolute magnitude. Similarly, Nyholm et al. [63] found no significant correlation between rise-time and peak luminosity in their sample.

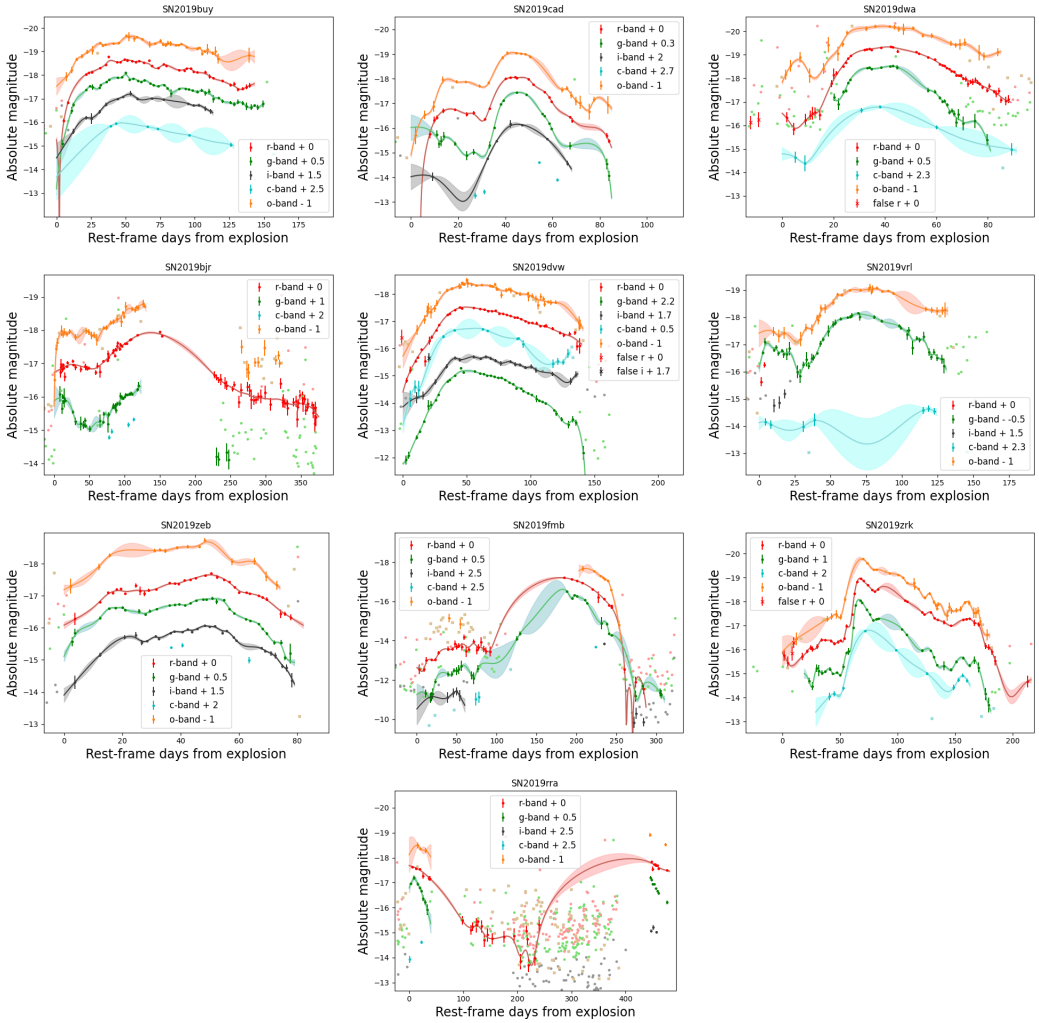

Figure 19. Peculiar subsample: in order displayed SNe are SN 2019buy (type Ib), SN 2019cad (type Ic), SN 2019dwa (type Ic), SN 2019bjr (type II), SN 2019 dvw (type II), SN 2019vrl (type II), SN 2019zeb (type II), SN 2019fmb (type IIn), SN 2019zrk (type IIn) and SN 2019rra (possible type II).

4.4 Peculiar subsample

A few peculiar SNe were mentioned before; now, it is time to examine them more closely. The whole peculiar subsample consists of ten SNe, presented in Figure 19. These SNe were not included when studying the rise-times of the sample of this thesis, but they are noted here as interesting examples of SN LC variety.

Many double or more peaks can be identified in this study sample. They are not common, but also not atypical among type IIn SNe [63] as interaction with the CSM

can be seen as an additional peak in the LC. However, not all of these double peaks observed belong to SNe IIn. SN 2019bjr, SN 2019cad, SN 2019dwa, SN 2019fmb, SN 2019vrl and SN 2019zrk are examples of these double-peaked SNe.

SN 2019cad and SN 2019dwa are type Ic SNe, and the first one has been studied previously in more detail by Gutiérrez et al. [68]. Because of these double peaks, the rise-times are significantly longer than the other type of Ic SNe at around 40-45 days. The reason behind the second peak is beyond the scope of this thesis, but general guesses could be interaction with CSM, a magnetar or multiple deposits of ^{56}Ni, as suggested by [68].

The longest rise-time in the sample is about 136 days and belongs to the type II SN 2019bjr. It is one of the double-peaked SNe. There are only two observations soon after the main peak in the r-band, but they are enough to give the general shape of the LC despite a long observation gap. No similar epochs are available in other bands to define the second peak, but a similar shape is visible. Double peaks are not common for type II SNe, so this is an extreme event, separating it from the majority of SNe II. There are a few other type II SNe that have had multiple peaks in their LC (for example, [69], [70], [71]), but they are the exception to the rule. On TNS, SN 2019bjr is marked as a type II-P, though the spectrum based on which it was classified is very noisy. The SN LC clearly lacks the plateau that is the defining feature of type II-P SNe.

Another double-peaked type II SN is SN 2019vrl, which also has an atypically long rise-time of about 70-80 days, depending on the band. It also has very distinct H-lines, making it a clear type II SN.

Though double peaks are not unheard of, when it comes to type IIn SNe, both SN 2019fmb and SN 2019zrk have peculiarly shaped LCs. They have somewhat two peaks, but the first one is very flat and faint, especially in the case of SN 2019fmb. With both of them, it was considered whether these epochs could, in fact,

be baseline with more dispersion, but the luminosity levels were significantly higher than previous epochs that did make up the baseline. In addition, ATLAS o-band detections were used in both cases during the first peak, making it more trustworthy.

Fransson et al. [72] investigated SN 2019zrk and concluded that the first fainter peak was not linked to the core-collapse. Instead, it was a long-lasting precursor. Strotjohann et al. [73] came to the same conclusion, and they also list SN 2019uo (Ibn), SN 2019bxq (IIn), SN 2019mom (IIn), SN 2019fmb (IIn), SN 2019aafe (IIn), SN 2019qny (IIn), SN 2019vkl (IIn) and SN 2019vts (IIn) that are also in this sample as having precursors. Since there isn't much data about the spectra or photometric follow-up in the sample of this thesis, no conclusions can be drawn. However, this possibility is worth noting. If these are precursors unrelated to the actual SN explosion, it will affect the estimated explosion epoch and, thus, the rise-times. Since this SN or the SN 2019fmb is not included in the mean rise-time calculation, it does not affect the results of this thesis.

SNe Ib in this sample are rather homogeneous, but one event stands out. While other rise-times are mostly below 30 days, SN 2019buy has a rise-time of about 50 days. As seen in the first panel of Figure 19, it is not a double-peaked SN but rather simply a very slowly rising one. Its LC also includes a few possible undulations.

Similarly, SN 2019dvw and SN 2019zeb are slowly rising SNe without multiple peaks, but they are classified as type II SNe. The first one has rise-times of about 50-57 days, and the second about 48-51 days, depending on the band.

One event, SN 2019rra, had to be ruled out from the sample. On TNS, it was classified as a type II SN based on an early time spectrum. The shape of the LC, however, is very peculiar, to say the least. A rise was captured in the g-band, and after the peak, all bands fell as expected. Around 100-250 days after the explosion, some possible detections occurred, but the error margins of these detections are so large that it is hard to be certain if these are real. Then, more than 400 days after

the explosion, detections with much smaller error margins were detected, and their absolute magnitude was even less than the initial peak (or around the initial peak since it wasn't recorded in other than g-band).

Because of the questionable LC shape, this event was excluded. SN 2019rra did not occur near the centre of its host galaxy, so AGN can be ruled out. One possible explanation could be another event occurring later very close by, in which case its LC could overlap with SN 2019rra, and the LC could actually represent two distinct objects.

5 Conclusions

In this thesis, a sample of 212 CCSNe of 7 distinct types was studied, and their rise-times and peak magnitudes were examined. The sample was divided into four subsamples based on the quality and quantity of photometric data available from the Zwicky Transient Facility and Asteroid to Terrestrial Last Alert System. Based on this data, LCs for these SNe were fitted with a Gaussian process, and their rise-times and peak absolute magnitudes were obtained.

Rise-time lengths found were in general order Ibn $<$ II $<$ Ic-BL $<$ Ic $<$ Ib $<$ IIb $<$ IIn. Especially type IIn SNe displayed a wide variety of LC shapes and rise-time lengths.

The difference between the rise-time lengths of different bands was also studied, and for the most part, the r-band with a longer effective wavelength had longer rise-times than the g-band. Additionally, the difference between these bands was that for the majority of the SNe, it was only a few days at most, but there were a few SNe with larger differences in rise-time lengths. Each SN, which had a longer rise-time in g-band than r-band, was checked, and at least in some of the cases, this was possibly due to lacking data, but it seems that this might not be the explanation for every SN.

To find if there were any correlations between rise-time length and peak absolute magnitude, their Pearson correlations were calculated. For the most part no significant correlations were found, but strong and very strong correlations were identified in SNe Ib, Ic-BL and IIb. Interestingly, these correlations were apparent only in r-band.

A subsample of peculiar SNe were identified in the sample, and though they were not the focus of the thesis, they were briefly discussed. They were not included in the rise-time study but were identified as potentially interesting objects for further research, though some had already been analysed previously. These SNe displayed multiple peaks and unusually long rise-times.

There is some room for improvement in any possible future research. The quality of the results of this thesis rely on heavily on the LCs so any improvement in the fitting would likely prove to be valuable. Such improvements could include reducing the scatter in the baselines to avoid false detections. This would also reduce scatter in the tail, though this doesn't have an effect on the main peak and, thus, rise-time and peak magnitude.

Another point of improvement is in the explosion epoch estimation since it is likely the largest source of error in this study. The method chosen here for the estimation was simple but not without its problems. Different limiting magnitudes can affect the explosion epoch, for example. Additionally, if the last reliable non-detection occurs long before the first detection, it is not of much use. Therefore, additional methods, such as comparing spectra to known spectra or fitting a polynomial to the LC in flux space, like in [18], could help constrain the explosion epoch.

Host extinction was not taken into account in this thesis, which does not affect the rise-time since it would be constant for each detection. However, it does affect the peak magnitude, so the peak magnitude vs. rise-time calculations would likely

benefit from performing host extinction correction.

Related topics could also be investigated in the future such as the LC post-peak to find possible additional energy sources and determine whether those have any effect on the rise-time or peak magnitude. Another would be to examine the colour evolution and the host galaxies of these SNe.

Acknowledgements

I would like to thank my supervisor Claudia Gutiérrez for guiding and supporting me through the journey that is writing a Master's thesis. It was not a simple or a quick task, but I have learned a great deal through it. I would also like to thank Seppo Mattila for the support in writing this thesis.

This research has made use of the ZTF forced-photometry service. The ZTF forced-photometry service was funded under the Heising-Simons Foundation grant #12540303 (PI: Graham).

This research has made use of the NASA/IPAC Extragalactic Database (NED), which is funded by the National Aeronautics and Space Administration and operated by the California Institute of Technology.

This work has made use of data from the Asteroid Terrestrial-impact Last Alert System (ATLAS) project. The Asteroid Terrestrial-impact Last Alert System (ATLAS) project is primarily funded to search for near-earth asteroids through NASA grants NN12AR55G, 80NSSC18K0284, and 80NSSC18K1575; byproducts of the NEO search include images and catalogs from the survey area. This work was partially funded by Kepler/K2 grant J1944/80NSSC19K0112 and HST GO-15889, and STFC grants ST/T000198/1 and ST/S006109/1. The ATLAS science products have been made possible through the contributions of the University of Hawaii Institute for Astronomy, the Queen's University Belfast, the Space Telescope Sci-

ence Institute, the South African Astronomical Observatory, and The Millennium Institute of Astrophysics (MAS), Chile.

References

[1] H. T. Janka *et al.*, Physics Reports **442**, 38 (2007).

[2] H.-T. Janka, T. Melson and A. Summa, Annual Review of Nuclear and Particle Science **66**, 341 (2016).

[3] V. Kalogera and G. Baym, Astrophysical Journal Letters **470**, L61 (1996).

[4] M. C. Bersten *et al.*, Nature **554**, 497 (2018).

[5] M. Modjaz, C. P. Gutiérrez and I. Arcavi, Nature Astronomy **3**, 717 (2019).

[6] F. Förster *et al.*, Nature Astronomy **2**, 808 (2018).

[7] D. O. Wells, S. L. Blatt and W. E. Meyerhof, Phys. Rev. **130**, 1961 (1963).

[8] M. E. Anderson, Nuclear Science and Engineering **62**, 511 (1977).

[9] R. Barbon *et al.*, Astronomy and Astrophysics Supplement **110**, 513 (1995).

[10] M. W. Richmond *et al.*, Astronomical Journal **107**, 1022 (1994).

[11] M. W. Richmond *et al.*, Astronomical Journal **112**, 732 (1996).

[12] P. J. Benson *et al.*, Astronomical Journal **107**, 1453 (1994).

[13] W. van Driel *et al.*, Publications of the Astronomical Society of Japan **45**, L59 (1993).

[14] M. Okyudo *et al.*, Publications of the Astronomical Society of Japan **45**, L63 (1993).

[15] N. V. Metlova *et al.*, Astronomy Letters **21**, 598 (1995).

[16] H. Mikuz, B. Dintinjana and T. Zwitter, IAU Circ **5796**, 2 (1993).

[17] F. Taddia *et al.*, Astronomy & Astrophysics **574**, A60 (2015).

[18] S. González-Gaitán *et al.*, Monthly Notices of the Royal Astronomical Society **451**, 2212 (2015).

[19] E. O. Ofek *et al.*, The Astrophysica Journal **789**, 104 (2014).

[20] K. Maeda *et al.*, The Astrophysical Journal **666**, 1069 (2007).

[21] J. C. Wheeler, Annals of the New York Academy of Sciences **617**, 8 (1990).

[22] A. Gal-Yam, Handbook of Supernovae 195 (2017).

[23] R. Minkowski, Publications of the Astronomical Society of the Pacific **53**, 224 (1941).

[24] J. C. Wheeler and R. Levreault, Astrophysical Journal **294**, L17 (1985).

[25] G. Hosseinzadeh *et al.*, The Astrophysical Journal **836**, 158 (2017).

[26] A. V. Filippenko, Annual Review of Astronomy and Astrophysics **35**, 309 (1997).

[27] A. V. Filippenko, in *Young Supernova Remnants*, Vol. 565 of *American Institute of Physics Conference Series*, edited by S. S. Holt and U. Hwang (AIP, 2001), pp. 40–58.

[28] R. Barbon, F. Ciatti and L. Rosino, Astronomy and Astrophysics **72**, 287 (1979).

[29] I. Arcavi *et al.*, Astrophysical Journal Letters **756**, L30 (2012).

[30] J. P. Anderson *et al.*, The Astrophysical Journal **786**, 67 (2014).

[31] L. Galbany *et al.*, The Astronomical Journal **151**, 33 (2016).

[32] N. E. Sanders *et al.*, The Astrophysical Journal **799**, 208 (2015).

[33] L. Dessart and D. J. Hillier, Astronomy & Astrophysics **622**, A70 (2019).

[34] A. V. Filippenko, Astronomical Journal **96**, 1941 (1988).

[35] E. M. Schlegel, Monthly Notices of the Royal Astronomical Society **244**, 269 (1990).

[36] A. Gal-Yam and D. C. Leonard, Nature **458**, 865 (2009).

[37] P. A. Crowther and L. J. Hadfield, The Messenger **129**, 53 (2007).

[38] W. D. Arnett *et al.*, Annual Review of Astronomy and Astrophysics **27**, 629 (1989).

[39] E. C. Bellm *et al.*, Publications of the Astronomical Society of the Pacific **131**, 018002 (2019).

[40] M. J. Graham *et al.*, Publications of the Astronomical Society of the Pacific **131**, 078001 (2019).

[41] J. L. Tonry *et al.*, Publications of the Astronomical Society of the Pacific **130**, 064505 (2018).

[42] K. W. Smith *et al.*, Publications of the Astronomical Society of the Pacific **132**, 085002 (2020).

[43] B. J. Shappee *et al.*, The Astrophysical Journal **788**, 48 (2014).

[44] N. M. Law *et al.*, Publications of the Astronomical Society of the Pacific **121**, 1395 (2009).

[45] N. Kaiser *et al.*, in *Survey and Other Telescope Technologies and Discoveries*, Vol. 4836 of *Society of Photo-Optical Instrumentation Engineers (SPIE) Conference Series*, edited by J. A. Tyson and S. Wolff (SPIE Digital Library, 2002), pp. 154–164.

[46] A. Gal-Yam, Science **337**, 927 (2012).

[47] F. J. Masci *et al.*, Publications of the Astronomical Society of the Pacific **131**, 018003 (2019).

[48] L. Shingles *et al.*, Transient Name Server AstroNote **7**, 1 (2021).

[49] D. J. Schlegel, D. P. Finkbeiner and M. Davis, The Astrophysical Journal **500**, 525 (1998).

[50] E. F. Schlafly and D. P. Finkbeiner, The Astrophysical Journal **737**, 103 (2011).

[51] T. Matsumoto and B. D. Metzger, The Astrophysical Journal **936**, 114 (2022).

[52] N. Elias-Rosa *et al.*, Astronomy & Astrophysics **686**, A13 (2024).

[53] E. Hubble, Proceedings of the National Academy of Science **15**, 168 (1929).

[54] J. A. Cardelli, G. C. Clayton and J. S. Mathis, Astrophysical Journal **345**, 245 (1989).

[55] F. Masci *et al.*, Generating Lightcurves from Forced PSF-fit Photometry on ZTF Difference Images, 2022.

[56] D. R. Young, "A script to plot the output returned from the ATLAS forced photometry service", `https://zenodo.org/doi/10.5281/zenodo.10978968`, 2020.

[57] S. Ambikasaran *et al.*, IEEE Transactions on Pattern Analysis and Machine Intelligence **38**, 252 (2014).

[58] C. Inserra *et al.*, The Astrophysical Journal **854**, 175 (2018).

[59] H. F. Stevance and A. Lee, Monthly Notices of the Royal Astronomical Society **518**, 5741 (2023).

[60] V. Borovitskiy *et al.*, arXiv e-prints arXiv:2006.10160 (2020).

[61] F. Taddia *et al.*, Astronomy & Astrophysics **621**, A71 (2019).

[62] P. J. Pessi *et al.*, Monthly Notices of the Royal Astronomical Society **488**, 4239 (2019).

[63] A. Nyholm *et al.*, Astronomy & Astrophysics **637**, A73 (2020).

[64] P. Virtanen *et al.*, Nature Methods **17**, 261 (2020).

[65] C. P. Gutiérrez *et al.*, The Astrophysical Journal **850**, 90 (2017).

[66] E. E. E. Gall *et al.*, Astronomy & Astrophysics **582**, A3 (2015).

[67] T. Faran *et al.*, Monthly Notices of the Royal Astronomical Society **442**, 844 (2014).

[68] C. P. Gutiérrez *et al.*, Monthly Notices of the Royal Astronomical Society **504**, 4907 (2021).

[69] S. Yang *et al.*, Astronomy & Astrophysics **646**, A22 (2021).

[70] T. Szalai *et al.*, Astronomy & Astrophysics **690**, A17 (2024).

[71] C. P. Gutiérrez *et al.*, Monthly Notices of the Royal Astronomical Society **496**, 95 (2020).

[72] C. Fransson *et al.*, Astronomy & Astrophysics **666**, A79 (2022).

[73] N. L. Strotjohann *et al.*, The Astrophysical Journal **907**, 99 (2021).

Appendix

The calculation of rise-time uncertainties are discussed more in this appendix. Both standard deviation of rise-time lengths and propagation of error relating to the explosion epoch were explored. The standard deviation was chosen as the uncertainty measure as it represents individual SNe better, and the sample of this thesis is quite heterogeneous.

Calculated uncertainties for rise-times are presented in table 11. For each type, subsample and band both sample standard deviation and error propagation are presented. The standard deviation was calculated of rise-time lengths, if there were more than 1 available. The error propagation was calculated from the explosion epoch uncertainties, using equation 16.

$$EP = \sqrt{e_1^2 + e_2^2 + e_3^2 + ...} \tag{16}$$

Here e_i is the uncertainty of a singular explosion epoch estimation, i.e. half of the time between first detection and the last deep non-detection before it. Error propagation was calculated separately for different bands because a SN usually did not have constrained rise in all bands. For example only one of the SNe Ib in the gold sample had a constrained rise in i-band. Therefore, only that SN was used in the error propagation calculation of i-band for the gold sample SNe Ib.

The individual uncertainties are rather small, but since there is a sum in the equation 16, the combined error propagation value is large for SNe II, where there are more SNe.

No error propagation could be calculated for the bronze subsamples of SNe Ib an IIn, since these SNe did not have a deep non-detection close enough to the first detection. In these cases the first detection was used as the explosion epoch, which offers only a lower limit to the rise-time. Thus, no uncertainty could be determined from the explosion epoch. If neither standard deviation nor error propagation could be calculated, it was marked as -/- in the table.

Similarly, some of the SNe II in the bronze sample had no deep non-detection close to the detection, but in some cases the non-detection was within 20 days of the

Table 11. Sample standard deviations (rounded up; in days)/error propagations (EP; in days) of each SN type in each band available. The peculiar subsample is not included in the results.

Type	subsample	g	r	i	c	o
		STD / EP	STD / EP	STD / EP	STD / EP	STD / EP
Ib	gold	4/5	4/5	-/3	-/3	6/5
	silver	0.8/4	11/0.5	-/0.5	no SNe	-/4
	bronze	8/-	6/-	no SNe	-/-	7/-
Ibn	gold	2/2	-/1	-/2	no SNe	0.5/2
	silver	-/4	6/4	-/4	no SNe	5/4
	bronze	no SNe	no SNe	no SNe	no SNe	no SNe
Ic	gold	7/6	6/7	4/4	no SNe	8/7
	silver	5/9	-/9	no SNe	no SNe	7/4
	bronze	no SNe	no SNe	no SNe	no SNe	no SNe
Ic-BL	gold	2/4	5/4	8/2	-/3	8/4
	silver	-/3	-/3	no SNe	no SNe	-/3
	bronze	no SNe	no SNe	no SNe	no SNe	no SNe
II	gold	6/11	7/12	9/8	6/7	7/12
	silver	5/11	5/12	2/2	no SNe	6/14
	bronze	4/11	7/10	-/7	5/4	5/11
IIb	gold	5.5/8.5	6.1/9.3	-/3.8	no SNe	5.8/5.9
	silver	-/1.2	-/1.2	no SNe	no SNe	no SNe
	bronze	no SNe	no SNe	no SNe	no SNe	no SNe
IIn	gold	16/9	19/9	17/6	15/4	20/9
	silver	0.9/2	-/0.4	no SNe	no SNe	14/4
	bronze	-/-	no SNe	no SNe	no SNe	5/-

first detection. In these cases there was no observed rise and the rise-time is only an upper limit, meaning that the uncertainty is also large. Only those SNe with a useful non-detection were used in the error propagation calculation.